Brigham Young University
BYU ScholarsArchive

All Theses and Dissertations

2013-08-27

Thermal Transport to Sessile Water Droplets on Heated Superhydrophobic Surfaces of Varying Cavity Fraction

Robb C. Hays
Brigham Young University - Provo

Follow this and additional works at: https://scholarsarchive.byu.edu/etd

 Part of the Mechanical Engineering Commons

BYU ScholarsArchive Citation

Hays, Robb C., "Thermal Transport to Sessile Water Droplets on Heated Superhydrophobic Surfaces of Varying Cavity Fraction" (2013). *All Theses and Dissertations*. 4241.
https://scholarsarchive.byu.edu/etd/4241

This Thesis is brought to you for free and open access by BYU ScholarsArchive. It has been accepted for inclusion in All Theses and Dissertations by an authorized administrator of BYU ScholarsArchive. For more information, please contact scholarsarchive@byu.edu, ellen_amatangelo@byu.edu.

Thermal Transport to Sessile Water Droplets on Heated Superhydrophobic Surfaces of Varying Cavity Fraction

Robb C. Hays

A thesis submitted to the faculty of
Brigham Young University
in partial fulfillment of the requirements for the degree of

Master of Science

Julie Crockett, Chair
R. Daniel Maynes
Brent W. Webb

Department of Mechanical Engineering

Brigham Young University

August 2013

Copyright © 2013 Robb C. Hays

All Rights Reserved

ABSTRACT

Thermal Transport to Sessile Water Droplets on Heated Superhydrophobic Surfaces of Varying Cavity Fraction

Robb C. Hays
Department of Mechanical Engineering, BYU
Master of Science

The hydrophobicity of a surface is defined as the degree to which it repels water molecules, and the internal contact angle that the droplet makes with the surface is a measure of the hydrophobicity. Contact angles less than 90° occur on hydrophilic surfaces, while contact angles greater than 90° occur on hydrophobic surfaces. If a surface's contact angle is greater than 120° the surface is commonly defined as superhydrophobic (SH). Superhydrophobicity is accomplished through a combination of microscale surface roughness and water repellant surface chemistry. The roughness creates cavities, or pockets, of vapor underneath the droplet which act to increase the effects of surface tension and lead to increased contact angles. The cavity fraction, F_c, of a surface is a measure of the surface roughness and is defined as the ratio of the projected cavity area to the projected total area of the surface.

This thesis investigates the effects of varying cavity fraction, F_c, and substrate temperature, T_s, on heat transfer to evaporating water droplets. Distilled water droplets of nominally 3 mm in diameter were placed on heated SH substrates of varying F_c (0.5, 0.8, and 0.95). A smooth hydrophobic surface was included in the experiments for comparative purposes. The temperature of the surface was held constant at temperatures ranging from 60 to 230°C while the droplet evaporated. Measurements of droplet temperature and size were taken throughout the evaporation process using CCD and infrared camera images. These images were analyzed to yield heat transfer rates for the various surface types and surface temperatures studied.

At temperatures below the saturation point of water, average droplet temperatures and heat transfer rates decrease with increasing cavity fraction. Differences in heat transfer rate between substrates increase with substrate temperature. Nusselt number decreases as cavity fraction is increased. Cavity fractions less than about 0.5 show only modest differences in Nusselt number between surfaces. As cavity fraction approaches unity, differences in Nusselt number become amplified between surfaces.

At temperatures above the saturation point of water, boiling behavior on SH surfaces deviates dramatically from that of smooth untextured surfaces. Average heat transfer rates decrease with increasing cavity fraction. Nucleate boiling is delayed to highter superheats than normal or is not observed. The Liedenfrost point is advanced to lower superheats as cavity fraction is increased. Similar heat transfer rates are observed beyond the Leidenfrost point.

Keywords: superhydrophobic, droplet evaporation, heat transfer

ACKNOWLEDGMENTS

I would like to thank Dr. Crockett, Dr. Maynes, and Dr. Webb for their guidance throughout this thesis project. Their advice and input were invaluable in all aspects of the project. I would also like to thank Joseph Prince and Ian Lavin for their help in manufacturing surfaces for the experiments and Matthew Searle for his help and input in performing experiments. I would also like to thank all of the members of the BYU FLYHT Lab for their input throughout the process. Thanks also go to my wife, Lakin, and son, Colby, for their patience and support while working on my degree.

This research was supported by the National Science Foundation (NSF) (Grant No. CBET-1235881).

TABLE OF CONTENTS

LIST OF FIGURES

CHAPTER 1. INTRODUCTION

Superhydrophobic (SH) surfaces have garnered recent interest in the scientific community owing to their potential in self-cleaning technology, drag reduction, and other applications. For many of these potential applications the thermal performance of a surface is also of major concern. The unique droplet roll-off behavior of SH surfaces makes them especially suited to heat transfer applications where dropwise heat transfer is of primary significance, as in steam condensers, or where frequent manual cleaning of the surface is undesirable. Characterization of dropwise heat transfer performance of SH surfaces is critical to the design of devices using this mode of thermal transport.

1.1 Superhydrophobic surfaces

Fig. (1.1) depicts the situation of a sessile liquid droplet, surrounded by a gas, resting on different types of solid surface. Young proposed that the contact angle, θ, that the droplet makes with a solid surface can be defined by the equation

$$\theta = \cos^{-1}\left(\frac{\gamma_{sg} - \gamma_{sl}}{\gamma_{lg}}\right) \tag{1.1}$$

where γ_{sg} is the surface tension between the solid and the gas, γ_{sl} is the surface tension between the solid and the liquid, and γ_{lg} is the surface tension between the liquid and the gas [1]. If θ is less than 90°, the surface is termed hydrophilic. If θ is greater than 90°, the surface is termed hydrophobic.

It was shown by Wenzel that a liquid droplet in contact with a micro-structured surface forms a new contact angle, θ_w, defined by the equation

$$\theta_w = \cos^{-1}(r\cos(\theta)) \tag{1.2}$$

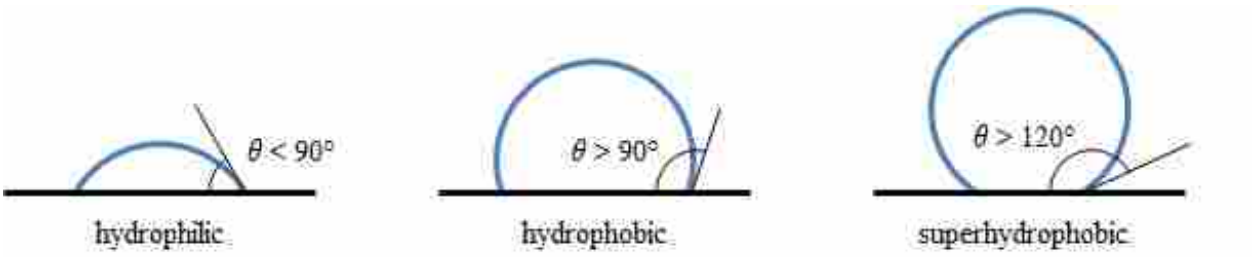

Figure 1.1: A sessile droplet, surrounded by a gas, resting on three different surface types with contact angle, θ, shown.

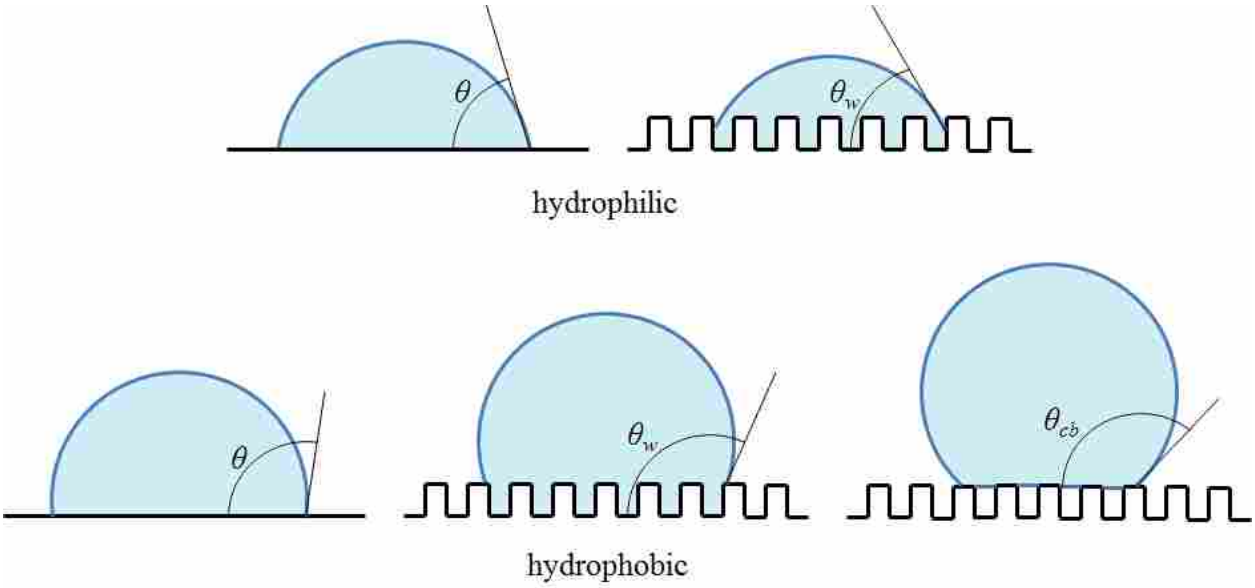

Figure 1.2: A sessile droplet resting on hydrophilic (top) and hydrophobic (bottom) surfaces. For the hydrophobic surfaces, the normal state (left), Wenzel state (middle), and Cassie-Baxter state (right) are all shown with their attendant increase in contact angle. For the hydrophilic surfaces, the normal state (left) and Wenzel state (right) are shown. The Cassie Baxter state does not occur for hydrophilic surfaces.

where r is the ratio of the total droplet-surface contact area to the projected surface area of the surface [2]. The effect of micro-structuring is to move the value of the contact angle further from 90°. This is shown in the top row of Fig. (1.2) where a droplet resting on a hydrophilic surface in the normal state and Wenzel state is shown. Note how the contact angle decreases between the normal and Wenzel states. Adding microstructuring renders already hydrophobic surfaces more hydrophobic (as shown in the bottom row of Fig. (1.2) and renders already hydrophilic surfaces more hydrophilic.

When the liquid becomes suspended on the tops of the microstructures such that vapor cavities are formed between microstructure features, the Cassie-Baxter state is reached. This state is described by another contact angle, θ_{cb}, defined by the equation

$$\theta_{cb} = \cos^{-1}(r(\cos(\theta)+1)-1) \tag{1.3}$$

with r and θ defined as before [3]. The smooth surface state described by Eqn. (1.1) along with the Wenzel and Cassie-Baxter states described by Eqns. (1.2–1.3) are depicted in the bottom row of Fig. (1.2) for hydrophobic surfaces. Note how the contact angle increases between the normal and Wenzel states and again between the Wenzel and Cassie-Baxter states.

While smooth surfaces have an upper limit in θ of approximately 120°, droplets in the Cassie-Baxter state can achieve contact angles greater than 120°. Surfaces that exhibit such high contact angles are termed superhydrophobic.

SH surfaces do occur in nature with the lotus leaf being the common example. SH surfaces can also be manufactured artificially using a variety of methods, though the basic principle behind manufacture is always creating microscale surface roughness with an outer hydrophobic layer. A common manufacture method uses photolithography and chemical etching to create ordered roughness patterns, such as rows of ribs or arrays of pillars, on a silicon wafer. This creates the microscale roughness necessary for the Wenzel state discussed above. Freshly-etched silicon wafers are naturally hydrophilic, so the addition of a hydrophobic top layer is necessary for the Cassie-Baxter state to occur. This is commonly accomplished by adding an adhesive layer to the bare silicon surface in addition to a hydrophobic coating. This adhesive layer is chosen so as to bond well to both the silicon and the hydrophobic coating. Chromium, aluminum, and other metals are common choices. Teflon and other fluorocarbons are commonly used as the hydrophobic coating. Fig. (1.3) shows a scanning-electron microscope image of a rib-patterned SH surface constructed using this method.

Droplet dynamics on superhydrophobic surfaces has been studied by various researchers [4–9]. Dupuis and Yeomans numerically investigated the dynamics of droplets moving across post-patterened SH surfaces. They found that droplet velocity increased with increased post spacing in the Cassie-Baxter regime [4]. Wang et al. studied droplet impingement on carbon nanotube SH

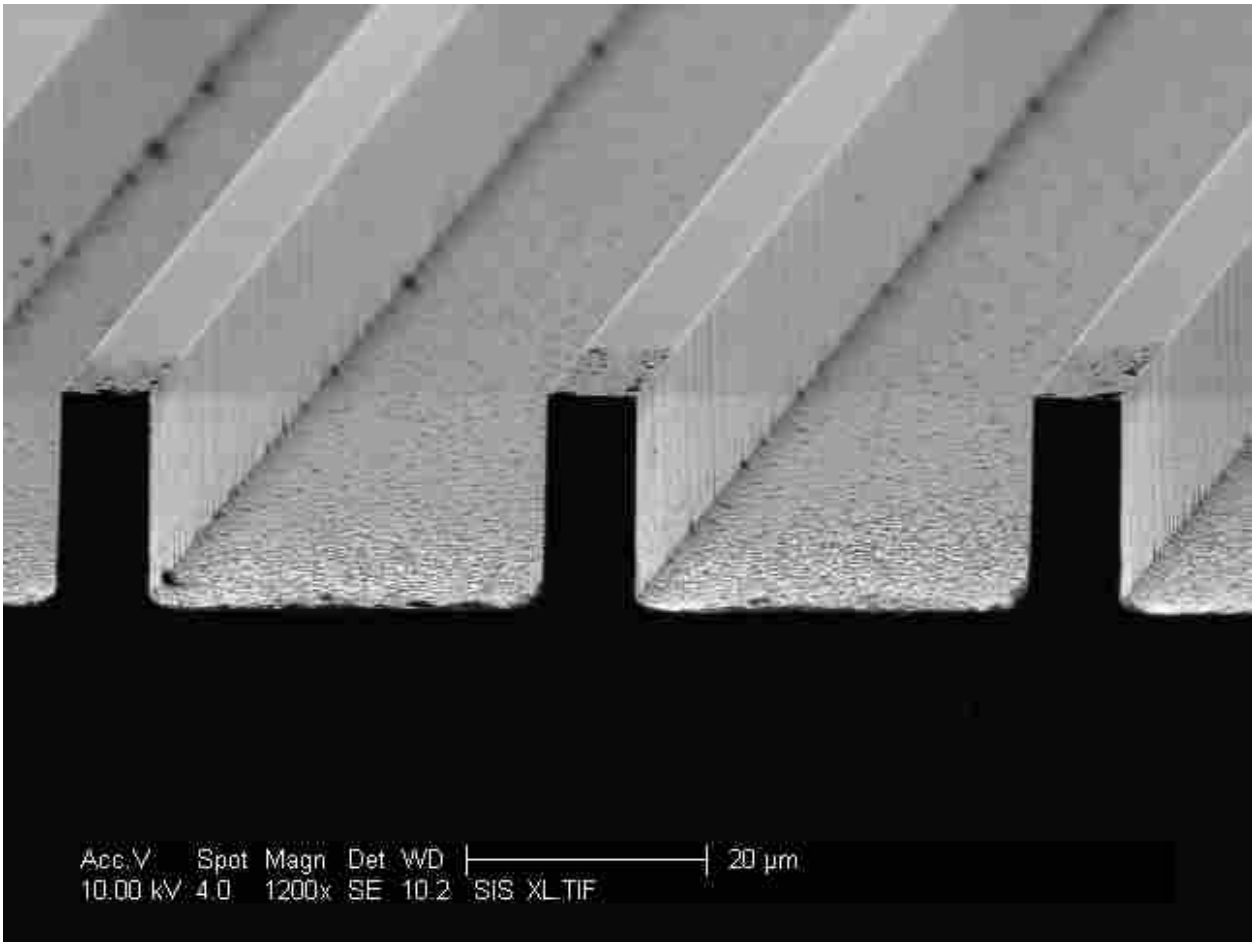

Figure 1.3: SEM image of a rib-patterend SH surface. Note the scale of the image.

surfaces. They observed that the dynamics of impingement and bouncing are heavily dependent on contact angle. Surfaces with higher contact angle bounce more readily than those with lower contact angle [7]. Jung and Bhushan created a criterion for determining the point at which transition between the Cassie-Baxter and Wenzel states occurs depending on droplet size and roughness topography [8].

In addition to droplet dynamics, flow over SH surfaces has been studied by numerous researchers [10–18]. Ou et al. conducted pressure drop experiments on SH surface channel flow. They observed significant pressure drop reductions (up to 40%) relative to smooth surface flow [10]. Ou and Rothstein also studied microchannel flow for rib-patterned SH surfaces using microparticle image velocimetry. They found that slip along the walls of the SH surface is the primary mechanism of drag reduction [11]. Davies et al. studied SH surfaces in parallel plate Stokes

flow and found significant reductions in frictional pressure drop relative to smooth-surface Stokes flow [12]. Daniello et al. conducted pressure drop and particle image velocimetry experiments for SH surface channel flow in the turbulent regime. They observed drag reductions approaching 50% [13]. It is important to note that while drag is reduced in the laminar regime on SH surfaces, varying levels of drag reduction have been observed on SH surfaces in turbulent flow regimes.

1.2 Heat transfer

Microstructuring of surfaces has implications not only for surface drag modification and self-cleaning properties but for heat transfer as well. The increase or decrease in solid-liquid contact area can affect the heat transfer behavior of the surface. What follows is a brief review of the heat transfer modes at play in a gas-liquid-solid system.

There are two main sources of heat transfer: molecular collisions within a medium or between neighboring mediums and radiative exchange of energy between surfaces. Heat transfer due to molecular collisions is termed either conduction, if bulk movement of the media are neglected, or convection, if the effects of bulk movement of media are included. Heat transfer due to radiative exchange of energy is termed radiation.

Fig. (1.4) shows an example of one-dimensional steady-state conduction through a solid wall of constant thermal conductivity with an applied heat flux, q''_x. The effect of the applied heat flux is to decrease the temperature within the wall linearly with x according to the equation

$$q''_x = k\frac{\Delta T}{L} \tag{1.4}$$

where k is the thermal conductivity of the wall material, ΔT is the temperature difference between the left and right surfaces of the wall, and L is the width of the wall [19].

Fig. (1.5) shows an example of convection between a solid wall and a fluid medium in motion across the surface. The heat flux, q'', from the surface to the fluid medium can be described by Newton's law of cooling,

$$q'' = h(T_s - T_\infty) \tag{1.5}$$

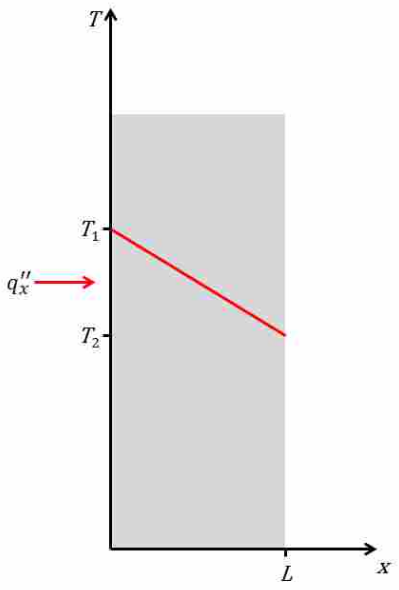

Figure 1.4: One-dimensional heat conduction in a plane wall with an applied heat flux at the boundary.

where h is the convection heat transfer coefficient, T_s is the surface temperature of the solid wall, and T_∞ is the temperature of the fluid medium [19]. The value of h is dependent on a variety of interconnected factors including the thermal conductivity, heat capacity, and velocity of the fluid and the temperature difference between the surface and the fluid as well as the surface geometry and the nature of the motion of the fluid.

Fig. (1.6) shows an example of radiative heat exchange between a solid wall within a vacuum and the surrounding walls. This type of heat transfer does not require physical contact between participating media as the energy is exchanged via electromagnetic radiation between surfaces instead of molecular collisions. The net heat exchanged between surfaces via radiation, q''_{rad} can be approximated by the equation

$$q''_{\text{rad}} = \varepsilon\sigma(T_s^4 - T_{\text{sur}}^4) \tag{1.6}$$

where ε is the emissivity of the solid wall, σ is the Stefan-Boltzmann constant, T_s is the temperature of the solid wall, and T_{sur} is the temperature of the surrounding surface [19]. Eqn. (1.6) assumes that the surroundings emit as a blackbody while the solid wall emits as a gray surface.

All three modes of thermal transport described above contribute to the overall heat transferred to and from sessile water droplets on heated surfaces. In addition to these mechanisms, heat

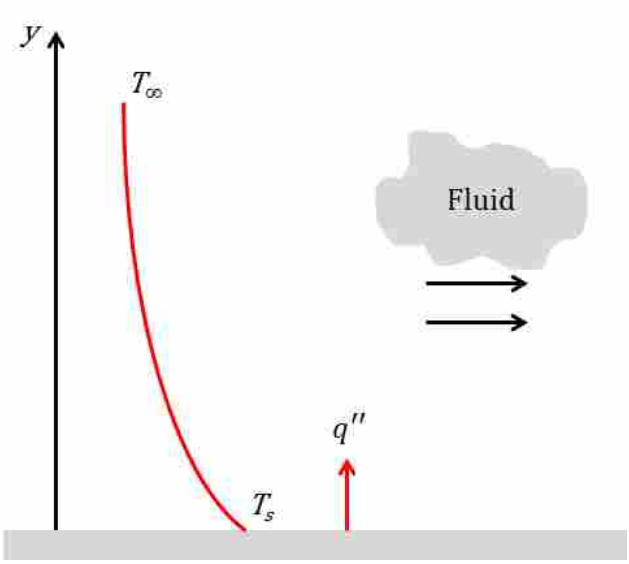

Figure 1.5: Convection between a solid wall and moving fluid.

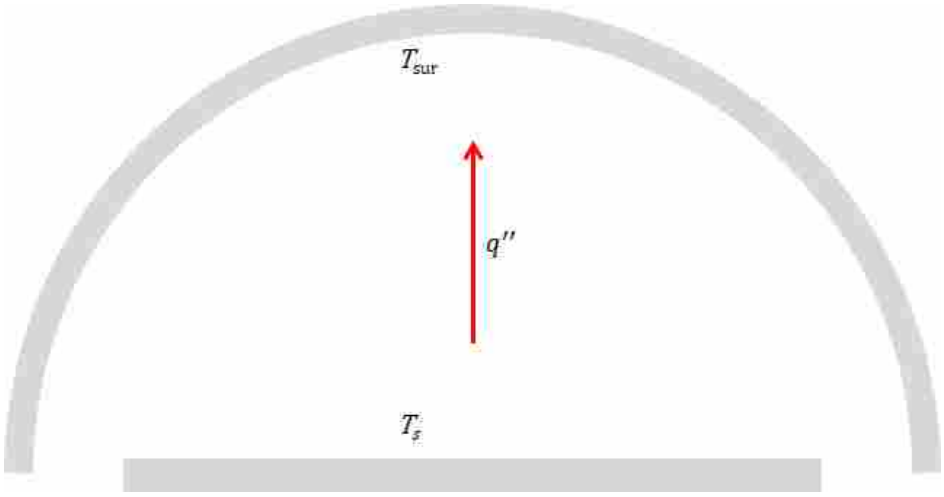

Figure 1.6: Radiation between a solid wall and surroundings within a vacuum.

can also be transferred away from the droplet through evaporation of the liquid in the droplet. As vapor is formed and transported away from the droplet by bouyancy, heat is lost from the droplet. Heat can also be stored within the droplet in the form of droplet temperature change. Fig. (1.7) shows the different heat transfer modes present in the situation of a sessile water droplet resting on a SH surface. Many interconnected factors including the temperature of the heated surface and the temperature and humidity of the surrounding air determine which modes of heat transfer are most significant in a given situation. Many researchers have conducted studies involving the transfer of

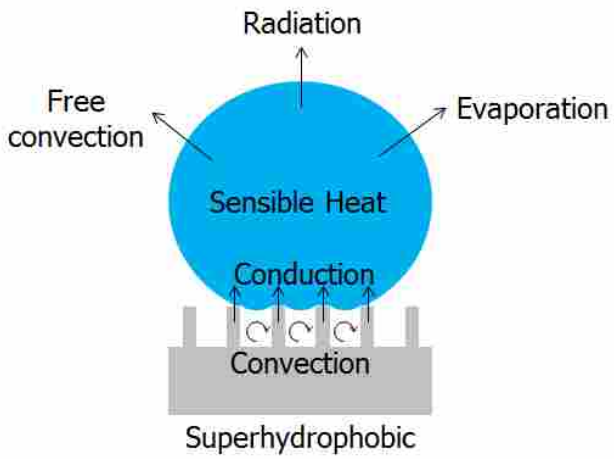

Figure 1.7: Depiction of a sessile droplet placed on a heated SHS. Convection and conduction occur at the base of the droplet, while free convection, radiation, and evaporative cooling occur at the upper surface of the droplet. Sensible heat is also produced throughout the droplet. The scale of ribs on SHS is exaggerated for clarity. The actual number of ribs contacting the droplet is on the order of 100.

heat between SH surfaces and water to determine how changing the hydrophobicity of a surface effects its heat transfer characteristics.

Pool boiling on SH surfaces has been studied by various researchers [20–23]. Takata et al. found that stable film boiling occurs at relatively low surface temperatures for SH surfaces and nucleate boiling is absent completely [20]. Phan et al. conducted experiments on hydrophilic and hydrophobic surfaces and found that nucleate boiling is delayed to higher superheats for more hydrophobic surfaces [21]. Pool boiling on superbiphilic (mixed superhydrophobic and superhydrophilic) surfaces was studied by both Betz et al. and Jo et al. They observed higher heat transfer rates on superbiphilic surfaces than for superhydrophilic surfaces. They concluded that the superhydrophobic sites on superbiphilic surfaces act as nucleation sites for nucleate boiling while the superhydrophilic sites act to increase the overall heat input to the pool [22, 23]. While the effects of hydrophobicity on both pool boiling and droplet boiling are expected to be similar, the fluid dynamics of heated droplets differ from those of heated pools. The heat transfer characteristics are therefore expected to differ between dropwise and pool boiling. This thesis studies droplet boiling and therefore applies more readily to situations where dropwise heat transfer is more dominant.

Droplet evaporation on SH surfaces has been studied by other researchers [24–27]. McHale et al. and Zhang et al. observed distinct modes of evaporation depending on the droplet regime.

Droplets in the Wenzel state exhibited a pinned contact line mode where the outer perimeter of the droplet contact surface remained fixed to the solid substrate. Droplets in the Cassie-Baxter state exhibited a constant contact angle mode where the contact line was free to recede and the contact angle remained fixed [24, 25]. Sobac and Brutin studied droplets freely evaporating on various surfaces. They observed that higher droplet contact angles corresponded to longer droplet evaporation times [26]. While much has been studied with regard to freely evaporating droplets on SH surfaces, most research has been qualitative in nature. In addition, little work has been done with regard to heated droplets, especially at surface temperatures above the saturation point of water where boiling occurs. This thesis quantitavely studies droplet evaporation on heated SH surfaces and therefore provides a more in depth characterization of the effects of hydrophobicity on dropwise heat transfer.

1.3 Project scope

All three modes of heat transfer discussed above (conduction, convection, and radiation) become significant at different points in the droplet evaporation process. In addition, it is to be expected that droplets at different surface states (i.e., Wenzel vs. Cassie-Baxter) would experience different amounts of heat transfer even for similar solid surface temperatures as the liquid comes into varying degrees of contact with the solid surface as shown in Fig. (1.2). The scope of this research is to explore experimentally how differing the microstructure topography of SH surfaces affects the heat transfer to sessile droplets at various wall temperatures. The results of these experiments characterize the effects of hydrophobicity on dropwise heat transfer at temperatures both above and below the saturation point of water. This expands upon the droplet evaporation studies of past researchers and also provides a needed link between pool boiling and dropwise heat transfer.

The rest of this thesis is organized into three main sections. The first two sections are standalone papers each with their own introduction, methods, results, and conclusions sections. The first section explores heat transfer through substrates at temperatures below the saturation temperature of water where the droplet itself does not experience boiling. The second section explores substrate temperatures above the saturation temperature of water where droplet boiling can occur. The final section discusses conclusions from both sections and suggests further work in this research area.

Two appendices are provided after the bibliography. Appendix A provides more detailed technical specifications of the experimental equipment used. Appendix B provides the MATLAB code used in gathering, analyzing, and presenting the data.

CHAPTER 2. THERMAL TRANSPORT TO DROPLETS AT SH SUBSTRATE TEMPERATURES BELOW THE SATURATION POINT

The content of the following chapter will be presented at the 2013 ASME IMECE conference this November and published in the proceedings of that conference. Upon publication, a full citation shall be listed here. The content of that publication is reproduced here and has been modified to fit the thesis requirements.

2.1 Introduction

Superhydrophobic (SH) surfaces exhibit internal contact angles with water in excess of 120°. This non-wetting behavior occurs in nature with such examples as the lotus leaf [28]. SH surfaces can exhibit internal contact angles with water of up to 177° [29]. Artificial SH surfaces are manufactured by combining microscale surface roughness with the application or coating of a non-wetting agent such as Teflon. SH surface manufacture methods to create uniform or random roughness include deep reactive ion etching, wax film growth, alumina gel film preparation, and vapor deposition of fluoroalkyl silanes among others [30].

The high contact angles exhibited by SH surfaces are higher than those currently possible via surface chemistry alone (e.g., coating with Teflon). The addition of microscale surface roughness acts to reduce the liquid-solid contact area. If the distance between roughness features is not too great, liquid at the surface will form menisci at the cavities between roughness features, creating alternating regions of liquid-solid interface and liquid-vapor interface as illustrated in Fig. (2.1). (Note that the figure is not to scale. The actual number of ribs contacting the droplet is on the order of 100.) This is termed the Cassie-Baxter state [3]. This state changes both the fluid flow and heat transfer behavior of liquids on the surface. The surface roughness of SH surfaces can be characterized by the cavity fraction, defined as the ratio of the projected area of the cavities

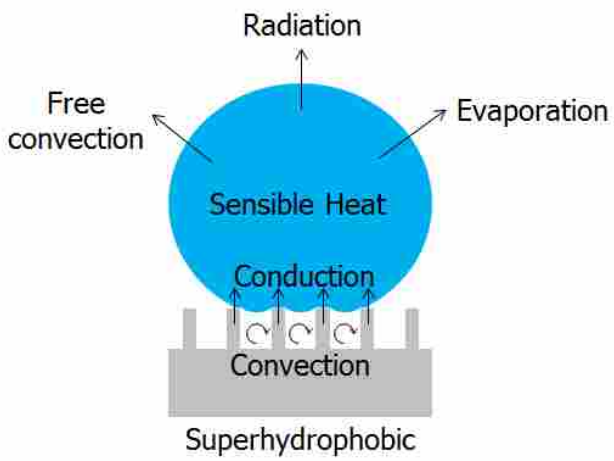

Figure 2.1: Depiction of a sessile droplet placed on a heated SH surfaces. Convection and conduction occur at the base of the droplet, while free convection, radiation, and evaporative cooling occur at the upper surface of the droplet. Sensible heat is also produced throughout the droplet. The scale of ribs on SH surfaces is exaggerated for clarity. The actual number of ribs contacting the droplet is on the order of 100.

(between roughness features) to the overall projected area of the surface. Higher cavity fractions correspond to lower liquid-solid contact area in the Cassie-Baxter state.

SH surfaces have a variety of potential applications, including drag reduction, self-cleaning surfaces, and MEMS actuation. Much has been studied in the area of fluid flow on SH surfaces. In contrast, relatively little work has been done regarding SH surface heat transfer behavior, especially with regard to droplet evaporation dynamics. A few investigators have reported on the behavior of evaporating droplets placed on hydrophilic and hydrophobic surfaces. The evaporation rate of a sessile droplet on a solid surface has been shown to be linearly proportional to the radius of the liquid-solid contact between the droplet and the SH surface [31, 32].

With the advent of artificial SH surfaces, investigators have observed distinct modes of droplet evaporation depending on surface type [24, 25]. The constant contact line mode is characterized by a pinning of the perimeter of the liquid-solid contact line such that the droplet-substrate contact area is constant throughout the evaporation process. This occurs throughout the evaporation of droplets on most hydrophilic surfaces and some hydrophobic and SH surfaces. It is also observed at the beginning and end of evaporation on most other SH surfaces. The constant contact angle mode is characterized by a retreat of the liquid-solid contact line accompanied by the maintenance of the liquid-solid interior contact angle. This is observed mostly for SH and hydrophobic

surfaces. The dominant mode of evaporation for a given surface is determined by its hysteresis [27]. Lower hysteresis surfaces (most SH surfaces) tend to exhibit the constant contact angle mode, corresponding to lower evaporation rates. Higher hysteresis surfaces (most hydrophilic and some SH surfaces) tend to exhibit the constant contact line mode, corresponding to higher evaporation rates.

A few researchers have reported on the interfacial heat flux during the evaporation process [26, 32–34]. It has been shown that smaller contact angles correspond to higher heat transfer rates and lower evaporation times [26].

Most of the past research in the area of droplet evaporation on SH surfaces has dealt with unheated droplets and disordered surface microstructures. The current research seeks to further characterize the heat transfer behavior of SH surfaces with regard to water droplet evaporation by providing more information on the influence of surface temperature and topography on droplet evaporation, especially as they relate to heat transfer rate. Experiments were conducted on various surface types and at various temperatures below the boiling point. Temporal variation of droplet geometry and temperature along with the influence of topography and surface temperature on evaporation rate and interfacial heat flux is presented.

The rest of the paper is divided into three sections. The first section outlines the experimental methods used to analyze an evaporating droplet, including hardware used, methods for collection of data, and data analysis. The next section presents results from the experiments and analysis of the data. The final section presents conclusions about the influence of surface temperature and topography on the interfacial heat transfer between sessile droplets and heated SH surfaces.

2.2 Methods

The substrates used in the current research include three different SH surfaces manufactured using photolithography, in addition to a smooth hydrophobic substrate. Fig. (2.2) is an SEM image of the type of SH surface used in the current research. The ribs on the SH surface used ranged in width from 2 to 30 μm and in height from 15 to 20 μm. The cavities between the ribs ranged in width from 30 to 38 μm.

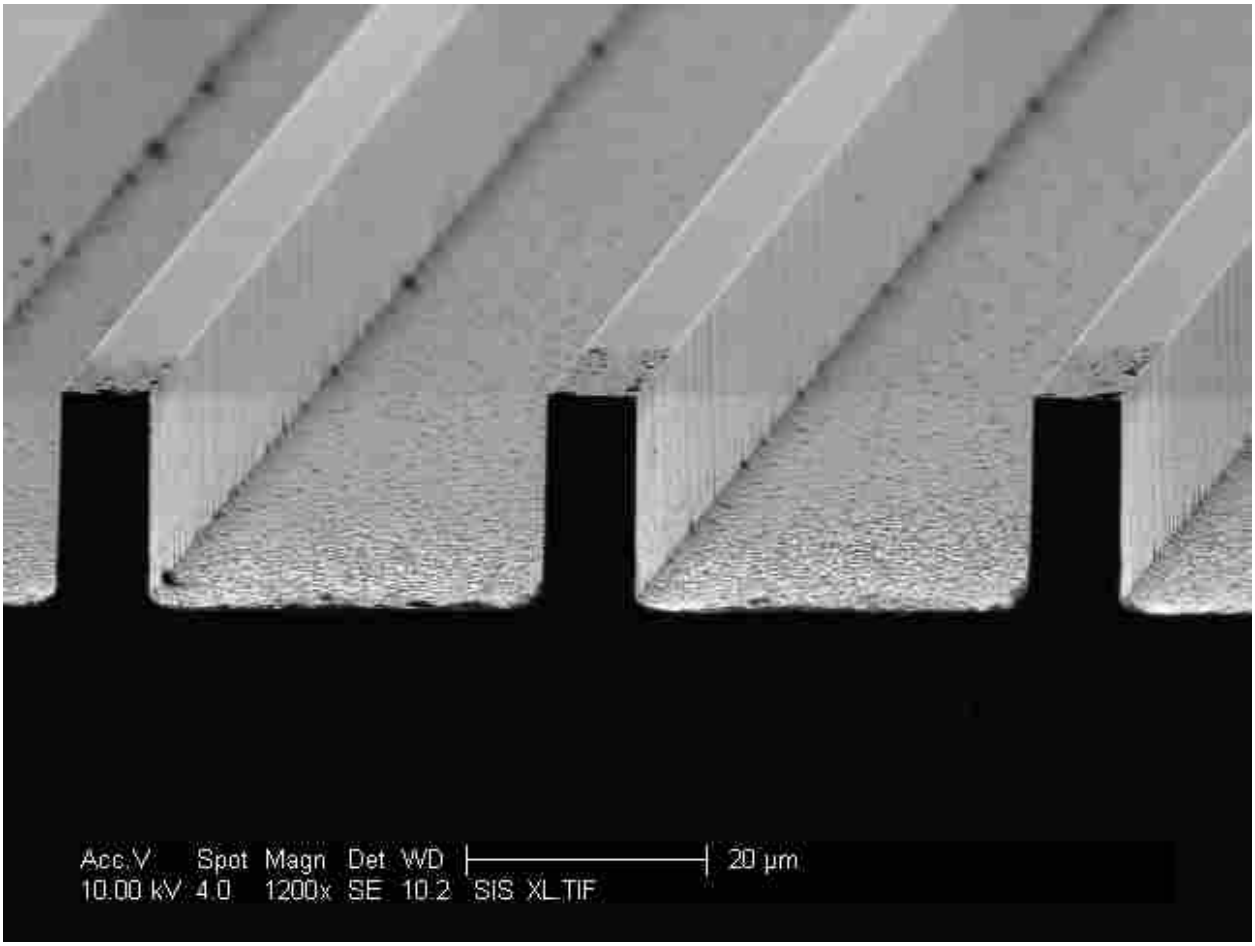

Figure 2.2: SEM image of the $F_c = 0.8$ SH surface used in this paper.

To manufacture such surfaces, patterns of parallel ribs of various sizes and spacing are first masked onto a silicon wafer using photoresist. The wafer is then etched to produce the pattern of alternating ribs and cavities shown in the image. Once the wafer is etched, Teflon is applied to the surface to make it superhydrophobic.

The cavity fraction, F_c, is a metric for SH surfaces that indicates the degree of superhydrophobicity of a given substrate. F_c is defined as

$$F_c = \frac{w_c}{w_c + w_r} \tag{2.1}$$

where w_c is the width of a cavity and w_r is the width of a rib. Higher cavity fractions indicate decreased water-solid interfacial contact and higher degrees of superhydrophobicity. The SH sur-

faces used in the current research are $F_c = 0.5$, 0.8, and 0.95, corresponding to initial interior static contact angles with water of approximately 120°, 123°, and 140°, respectively. In addition to the three SH surfaces, a smooth substrate coated with Teflon (i.e., $F_c = 0$), with an initial interior contact angle with water of approximately 108° was used as a control in the current research.

The experiments performed in the current research consist of monitoring a sessile water droplet nominally 3 mm in diameter undergoing evaporation on a heated silicon wafer substrate. The measurements required for heat transfer analysis are dictated by the particular heat transfer model used. Fig. (2.1) depicts the present situation of a sessile water droplet placed on a horizontal substrate. Heat is exchanged between the substrate and the droplet via conduction through the ribs and convection and radiation through the cavities. Heat is transferred from the droplet to the ambient air via convection, radiation, and mass transfer of water vapor.

Applying Newton's Law of Cooling to the external droplet-air interface yields

$$\dot{q}_{conv} = h_{conv} A_u (T_d - T_\infty) \tag{2.2}$$

where h_{conv} is the convective heat transfer coefficient for the external water-air interface, A_u is the exposed upper-surface area of the droplet, T_d is the droplet temperature, and T_∞ is the ambient air temperature.

Applying the Stefan-Boltzmann Law to the droplet-surroundings radiative heat transfer yields

$$\dot{q}_{rad} = \varepsilon \sigma A_u (T_d^4 - T_{surr}^4) \tag{2.3}$$

where ε is the droplet surface emissivity, σ is the Stefan-Boltzmann constant, and T_{surr} is the surface temperature of the surroundings.

The sensible heat change within the droplet is given by

$$\dot{q}_{sens} = c_p \rho V \frac{dT_d}{dt} \tag{2.4}$$

where c_p is the specific heat capacity of water at the droplet temperature, ρ is the water density, V is the droplet volume, and dT_d/dt is the time rate of change of the droplet temperature.

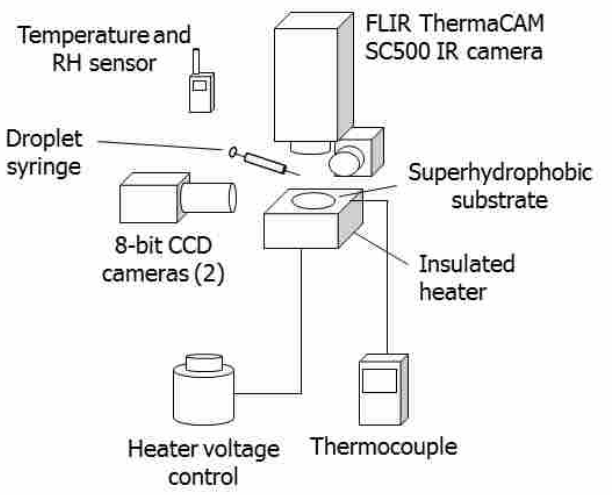

Figure 2.3: Experimental setup used for this paper. Heated substrate apparatus is shown along with cameras and other sensors used for measurement.

Heat loss due to mass transfer of water vapor from the droplet surface can be represented by

$$\dot{q}_{evap} = h_{fg}\rho\frac{dV}{dt} \tag{2.5}$$

where h_{fg} is the latent heat of vaporization of water at the droplet temperature and dV/dt is the time rate of change of the droplet volume.

The overall heat transfer rate from the substrate to the droplet can be representated by

$$\dot{q}_s = h_s A_c (T_s - T_d) \tag{2.6}$$

where A_c is the projected contact area between the droplet and the substrate, T_s is the substrate temperature, and h_s is an overall coefficient representing all modes of heat transfer between the substrate and the droplet.

From Eqns. (2.2–2.6) an experiment was designed to measure all of the relevant variables. Fig. (2.3) shows the experimental setup used in the present research. A patch heater is affixed to the underside of an aluminum block which is then seated in a block of insulating foam. The heat output of the patch heater is controlled by a voltage transformer. Various silicon wafers are affixed to the top of the heated aluminum block using thermal paste for good thermal contact.

The silicon substrate temperature, T_s, is measured using a K-type thermocouple embedded 3 mm below the top surface of the aluminum block. This sensor has an uncertainty in temperature of $\pm 1.5^{\circ}$C. A correlation between the temperature measured by this thermocouple and the true temperature of the upper surface of the substrate is found using a flat-black painted silicon wafer and an infrared camera oriented normal to the surface of the wafer. The heater was set to various steady-state temperatures, and a linear relationship between the temperature observed by the thermocouple and the temperature observed by the infrared camera is found. The linear fit between the thermocouple and IR camera data used in the current research has a coefficient of determination of $R^2 = 0.9998$.

For the current research, the substrate is heated to various steady-state temperatures ranging from 60 to 100°C. A single droplet of water, nominally 3 mm in diameter, is placed on the heated silicon substrate using a syringe. The geometry of the droplet through time is observed using two CCD cameras oriented perpendicularly to one another (one aligned parallel to the microribs and the other transverse to the microribs) and parallel with the surface of the substrate. A_u, A_c, and V are then determined from the resulting droplet images.

An infrared camera is placed normal to the substrate surface and focused on the top of the evaporating droplet to measure the droplet surface temperature, T_d, through time. This temperature is not to be understood as an average or minimum droplet temperature but, rather, a representative droplet temperature. The uncertainty in T_d introduced by the infrared camera is nominally $\pm 3.2^{\circ}$C. The ambient air temperature, T_∞, is measured using a thermocouple with an uncertainty of $\pm 0.4^{\circ}$C.

An analysis of the relative importance of the heat transfer terms in Eqns. (2.2–2.5) was conducted using the data gathered from this experimental setup. Fig. (2.4) shows the typical relative magnitude of each term for the entire evaporating scenario. Plotted on the y-axis is a ratio of the heat transfer rate from an individual heat transfer mode to the overall heat transfer rate. Plotted on the x-axis is the time normalized by the total evaporation time of the droplet. During the initial heat-up period, sensible heat is significant, but after a short time (quasi-steady state), the heat transfer due to mass transfer of water vapor dominates all other terms, representing greater than 95% of the total heat loss. Consequently, the heat transfer due to convection and radiation from the upper surface of the droplet along with the sensible heat change within the droplet, represented by Eqns. (2.2–2.4) respectively, is neglected in subsequent results and analysis.

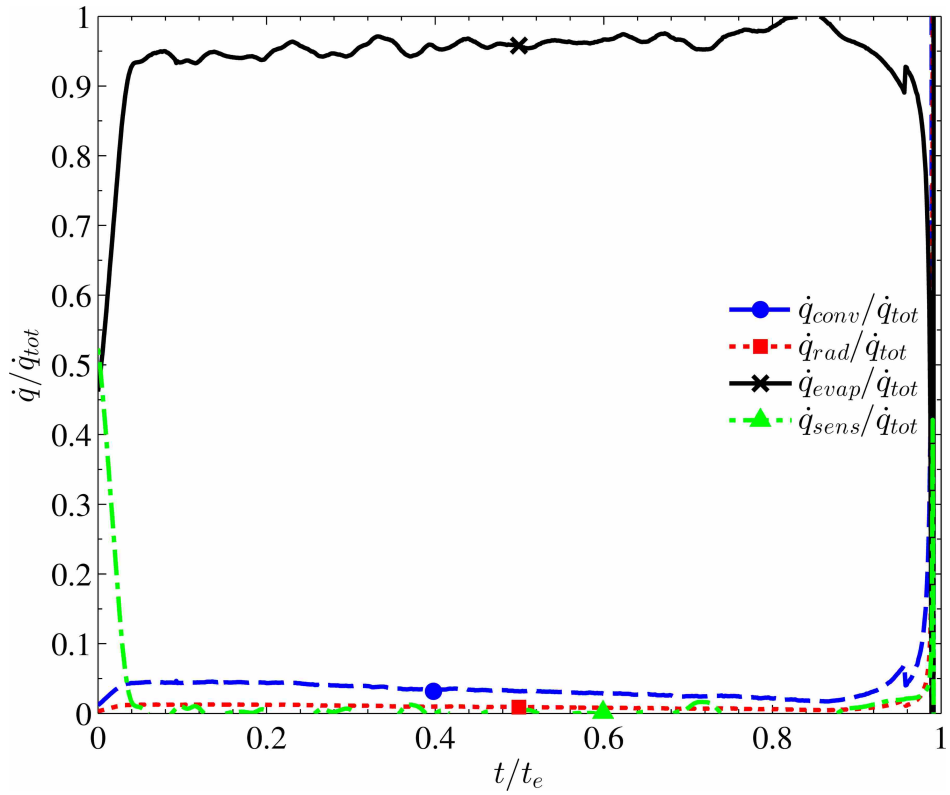

Figure 2.4: Ratio of each mode of heat loss to the total heat loss as a function of time normalized by the total evaporation time for a representative scenario.

Conservation of energy can be applied to the droplet by combining Eqns. (2.5) and (2.6) to yield

$$h_s A_c (T_s - T_d) = h_{fg} \rho \frac{dV}{dt} \tag{2.7}$$

or, solving for h_s,

$$h_s = \frac{h_{fg} \rho dV/dt}{A_c (T_s - T_d)} \tag{2.8}$$

h_s is a convection coefficient representating the effectiveness of the substrate in transferring heat to the droplet.

The experiments were conducted three times at each substrate temperature and for each substrate type. The CCD camera data were compiled and analyzed in MATLAB using standard image processing algorithms, and the IR camera data were analyzed using the camera's native software.

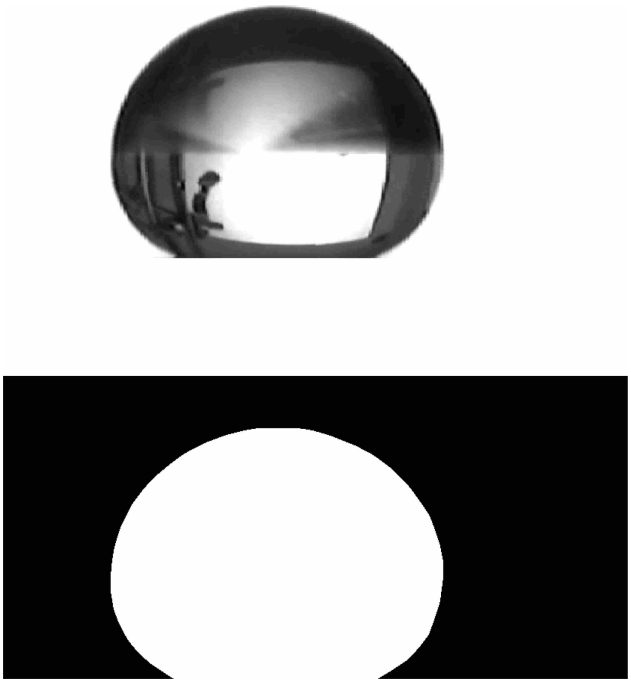

Figure 2.5: CCD image of a droplet resting on the $F_c = 0.95$ substrate (top) and the binary transformation of this image after processing (bottom).

Analysis of the CCD camera data begins with segmentation of the images of the liquid droplets. A grayscale intensity threshold is determined that distinguishes the droplet from the rest of the image. A binary operation is applied, using this threshold, to isolate the droplet in the image. Noise is then eliminated by comparing the pixel counts of the various objects in the image, as the droplet should be the largest object in the image. The resulting binary droplet images are then processed to extract geometry. Fig. (2.5) shows a raw CCD image of a droplet along with its binary transformation after going through the image processing algorithm.

The droplet images can be thought of as a stack of horizontal rows of pixels that form the droplet shape. Droplet volume is calculated by first finding the distance, in pixels, between the left and right edges of the droplet at each horizontal ”slice” of the droplet. This number of pixels can be converted to a physical distance by using a calibration constant determined by imaging an object of known size. This calibration image can be analyzed to find a conversion between numbers of pixels in an image and physical distances. If the droplet is assumed to be axisymmetric, the volume of each slice is found from

$$V_i = \frac{\pi d_i^2 h_p}{6} \tag{2.9}$$

where d_i is the distance, in physical units, between left and right droplet edges at a particular vertical pixel location, and h_p is the height, in physical units, of one pixel. The volume of the droplet is then found by summing the individual volumes of each "slice" of the droplet. Any asymmetry in the droplet can be accounted for by averaging together the volumes found by each camera's image. The difference in measured volume between the two perpendicular camera views was always less than $\pm 2\%$.

The projected droplet-substrate contact area can be found by assuming an elliptical droplet footprint on the substrate and using

$$A_c = \frac{\pi d_l d_r}{4} \tag{2.10}$$

where d_l and d_r is the distance between the the left and right edges of the droplet at the droplet-substrate interface for the left and right camera views, respectively. An alternative method would be to assume the droplet footprint is circular and average the contact areas found using each camera view independently. The difference between the area found using the method of Eq. (2.10) and this second method is on the order of $\pm 0.1\%$. The difference between d_l and d_r depends on the substrate. More anisotropic surfaces will yield larger differences. For example, the $F_c = 0.95$ substrate (anisotropic due to the microribs) yields a difference between d_l and d_r of nominally 10%. The smooth hydrophobic substrate (ideally isotropic) yields a difference of nominally 1%.

The droplet-substrate interior static contact angle is found by first fitting an ellipse to the edges of the droplet near the SH surface using a least-squares fitting method. The tangent lines to this ellipse at the left and right edges where the droplet meets the SH surface are then found. The contact angle at the left and right edges is then found by taking the inverse tangent of the slope of these tangent lines. The angles found for the left and right edges in each camera image are then averaged to find an overall static contact angle.

2.3 Results

In general, the volume of sessile water drops undergoing evaporation follows an inverse function with time. Evaporation occurs most rapidly at the beginning of the transient process, when the droplet is largest, and the rate decreases as the droplet becomes smaller in size. This occurs because the droplet evaporation rate is driven by the amount of heat the droplet receives from

the substrate. As the droplet decreases in size, less of the droplet is in contact with the substrate and, consequently, less heat is transferred to the droplet from the substrate. This results in higher evaporation rates earlier in the evaporation process when more of the droplet is in contact with the substrate. If the substrate is unheated, the driving force for evaporation is the difference in water concentration between the droplet surface and the ambient air, as shown in Fick's law of diffusion [35]. As the substrate is heated, however, the substrate temperature itself becomes the important variable in droplet evaporation. The heat added to the evaporating droplet serves to accelerate the evaporation process, and the effects of evaporative cooling keep the droplet temperature well below that of the substrate. The contact area between the droplet and the substrate tends to be a linear function of time, which is analagous to the D^2 law of suspended evaporating drops [36].

Fig. (2.6) shows the droplet temperature as a function of time for a single test case of each substrate studied at a constant substrate temperature of 80°C. This is representative of what occurs for all cases where substrate temperature is less than the saturation temperature of water. There is an initial period of temperature rise immediately after the droplet is first placed on the heated substrate. This time is on the order of 10 s. This is followed by a relatively long period of nominally constant droplet temperature. This constant T_d regime is the focus of the current research. T_d is lowest for the $F_c = 0.95$ case and highest for the smooth hydrophobic case. In general, T_d decreases with increasing F_c. Toward the end of the droplet's evaporation process, the droplet temperature experiences drastic changes. In some cases, the droplet cools and then heats up. In other cases, the droplet merely cools immediately before complete evaporation. The SH surfaces almost always follow the trend of cooling and then heating right before evaporation. The smooth hydrophobic substrate tends to follow the trend of cooling without reheating but sometimes exhibits the cooling-heating cycle observed for SH surfaces. However, the temperature fluctuation and variability near the end of the process is not the focus of this paper. Of important note, however, is that droplet temperature remains relatively constant for most of the evaporation process and that droplet temperature decreases with increasing cavity fraction.

Fig. (2.7) shows the droplet volume as a function of time for the same representative cases depicted in Fig. (2.6). The data for this and the following figures were truncated by defining $t = 0$ as that condition when the droplet volume is equivalent to that of a sphere of diameter 3 mm. This allows for direct comparisons of the data between different experiments and substrates and has the

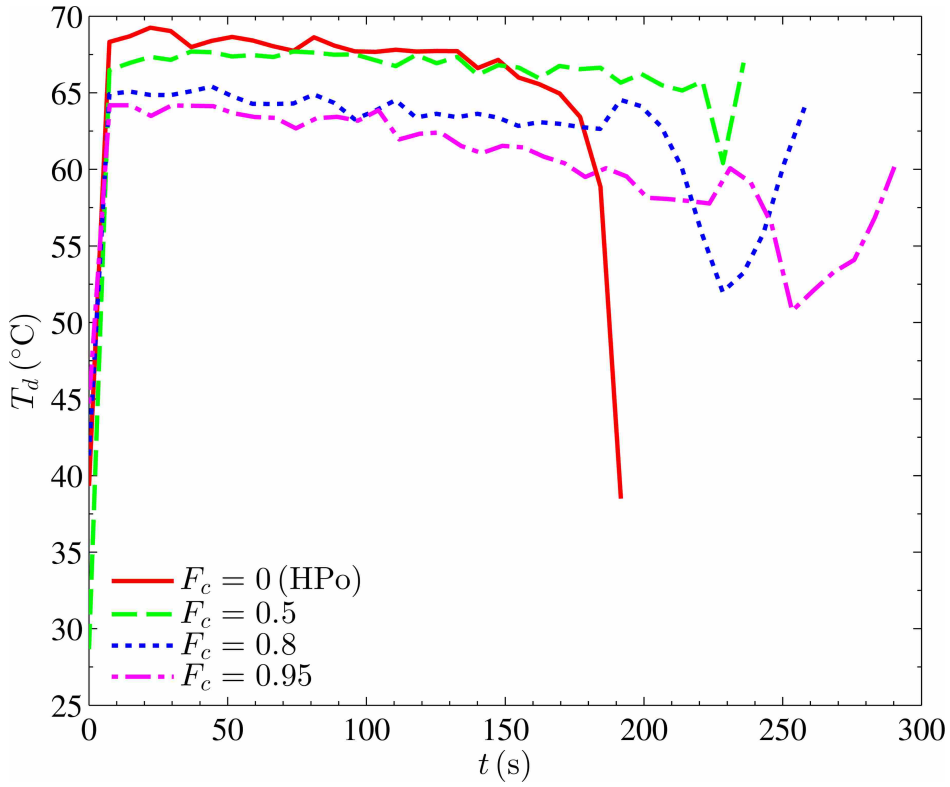

Figure 2.6: Transient droplet temperature as a function of time for substrate temperature of nominally 80 °C and for all substrates considered.

added benefit of removing the initial temperature transients observed in Fig. (2.6). The droplet volume decreases continuously with time, with dV/dt decreasing as evaporation progresses. This behavior was typical for all substrate types and temperatures. Of note is the difference in initial dV/dt between the various substrates. dV/dt is greatest for the smooth hydrophobic substrate and least for the $F_c = 0.95$ substrate. In general, as F_c is increased, the initial dV/dt decreases, leading to increased droplet lifetimes. This decrease in dV/dt with increasing F_c can explained by the overall decrease in direct liquid-solid contact with increasing F_c. Decreased contact yields a decrease in heat conduction between the substrate and the droplet and an overall decrease dV/dt.

Fig. (2.8) provides the projected droplet-substrate contact area as a function of time for the same representative cases as the previous two figures. The contact area decreases with time nearly linearly, although sometimes in a step-wise fashion. For SH surfaces, this is explained physically by the presence of microribs on the surface. As the droplet evaporates, it is pinned temporarily at the ribs until surface tension overcomes the pinning forces and the droplet then

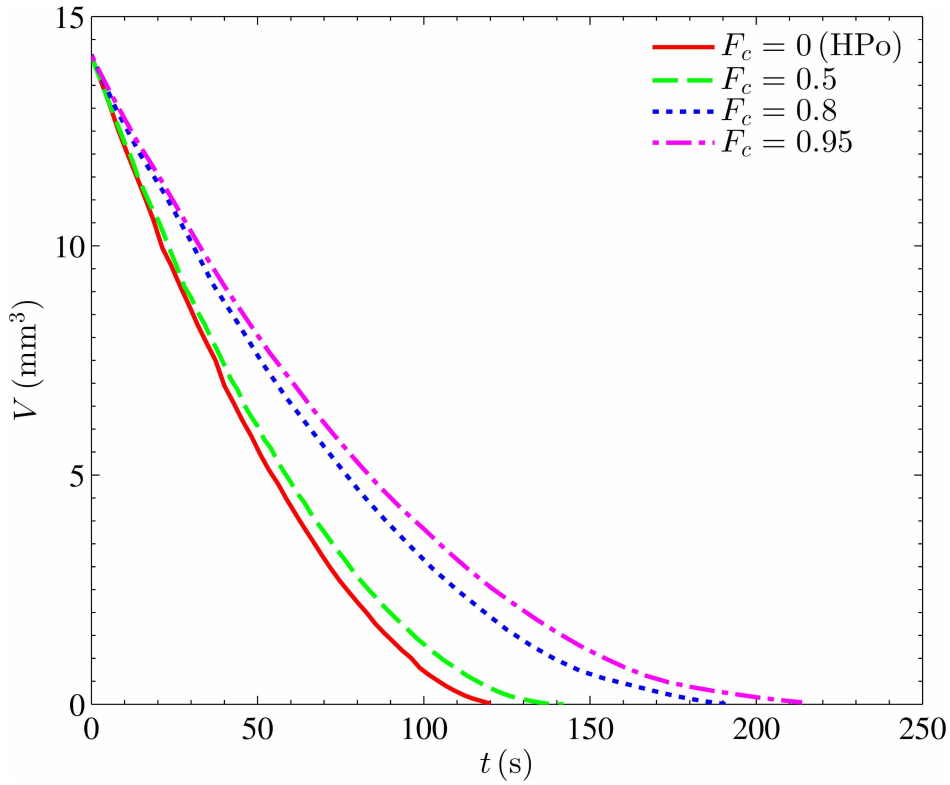

Figure 2.7: Transient droplet volume as a function of time for substrate temperature of nominally 80 °C and for all substrates considered.

pins at another set of ribs. This behavior can be readily deduced from the depiction in Fig. (2.1) of a droplet resting on a SH surface. For the smooth hydrophobic cases this behavior is more likely caused by imperfections in the surface of the substrate. The droplet pins and unpins at these imperfections, much in the same way as the SH surface cases, but the behavior is much more chaotic and unpredictable.

Also of note in the figure is the difference in initial contact area between the various substrates. As F_c is increased, the initial A_c is decreased. This in part explains the increased droplet lifetimes because less heat is transferred from the substrate to the droplet as A_c becomes smaller.

Fig. (2.9) shows the droplet contact angle, θ, as a function of time for the same representative cases shown in Figs. (2.6–2.8). The contact angle remains relatively constant over most of the evaporation process until near the end of the droplet's life, when the droplet becomes pinned to the surface and contact angle decreases rapidly. This behavior is typical across all substrate types

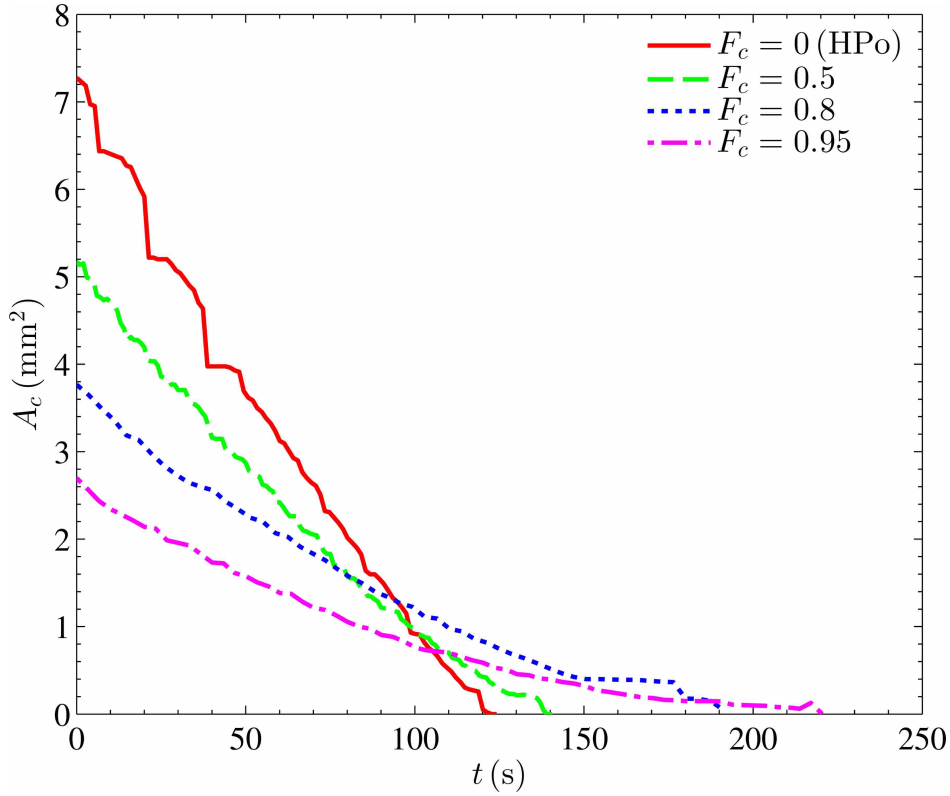

Figure 2.8: Transient projected droplet-substrate contact area as a function of time for substrate temperature of nominally 80 °C and for all substrates considered.

and temperatures and is not dependent on substrate temperature. The nearly constant θ regime is of most relevance to this paper.

Of particular note in the figure is the increase in initial θ with F_c. This explains the differences in A_c observed in the previous figure. Also of note are the observed fluctuations in θ with t, which are most prominent in the smooth hydrophobic case. This is another manifestation of the pinning-depinning behavior observed in Fig. (2.8).

For convenience in working with and drawing conclusions from the data, indirect measurements of the droplet evaporation (such as evaporation time and Nusselt number) were calculated by first truncating the original data to remove the temperature transients at the end of the droplet's life. This is in addition to the volume-based truncation mentioned previously. To aid in calculating dV/dt, the droplet volume data were smoothed using a linear least squares, second degree polynomial local regression. The regression was localized over no less than 1/4 of the span of the V data. The smoothed V curves agreed with the original V data very well with a coefficient of

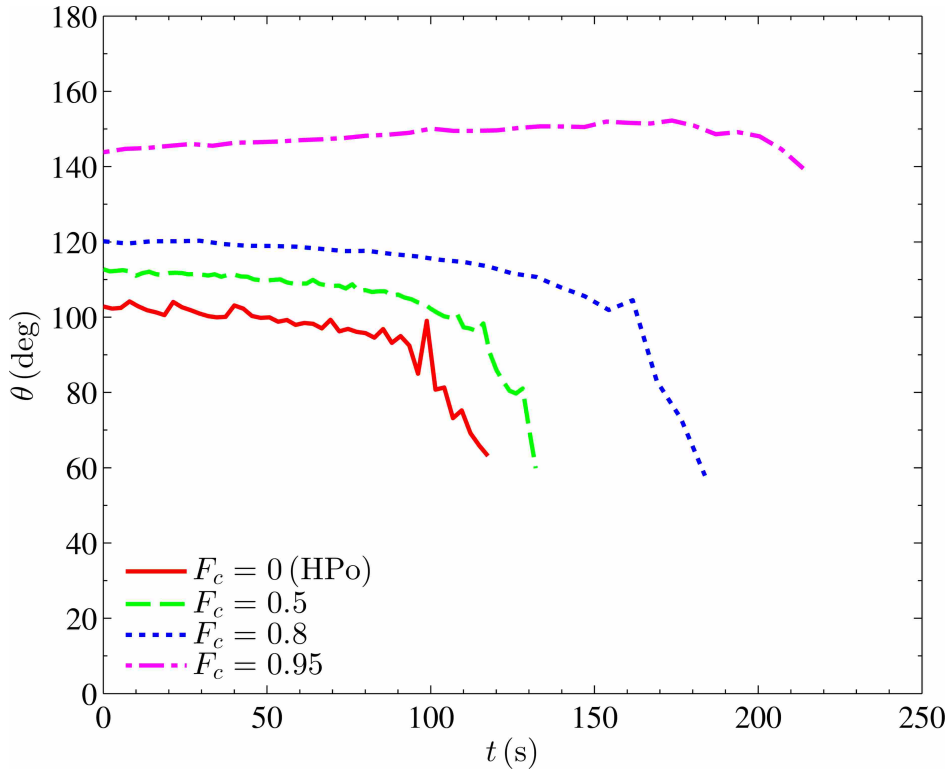

Figure 2.9: Transient internal droplet-substrate contact angle as a function of time for substrate temperature of nominally 80 °C and for all substrates considered.

determination of approximately $R^2 = 0.9999$. All other data were used as-is in calculating these indirect measurements.

Fig. (2.10) shows the total evaporation time as a function of substrate temperature for all substrates and temperatures studied. As the substrate temperature increases, the evaporation time decreases due to an increase in heat transfer to the droplet. The evaporation time decreases as F_c decreases, again due to a increase in heat transfer to the droplet. This is explained physically by the increase in both projected droplet-substrate contact area and physical droplet-substrate contact as depicted in Fig. (2.11). Power-law curve-fits for each substrate were determined and included in Fig. (2.10). The increase in heat transfer for lower F_c is reflected by an increase in the power on T_s for decreasing F_c. In other words, the substrate temperature plays an increasingly important role in the heat transfer rate as F_c decreases. Also of note is that the SH surface curves intersect at about $25°C$ (ambient temperature) when extrapolated off the left side of the figure. Droplet evaporation times are expected to collapse as the surface temperature approaches ambient because the substrate's influence on evaporation becomes negligible at this condition.

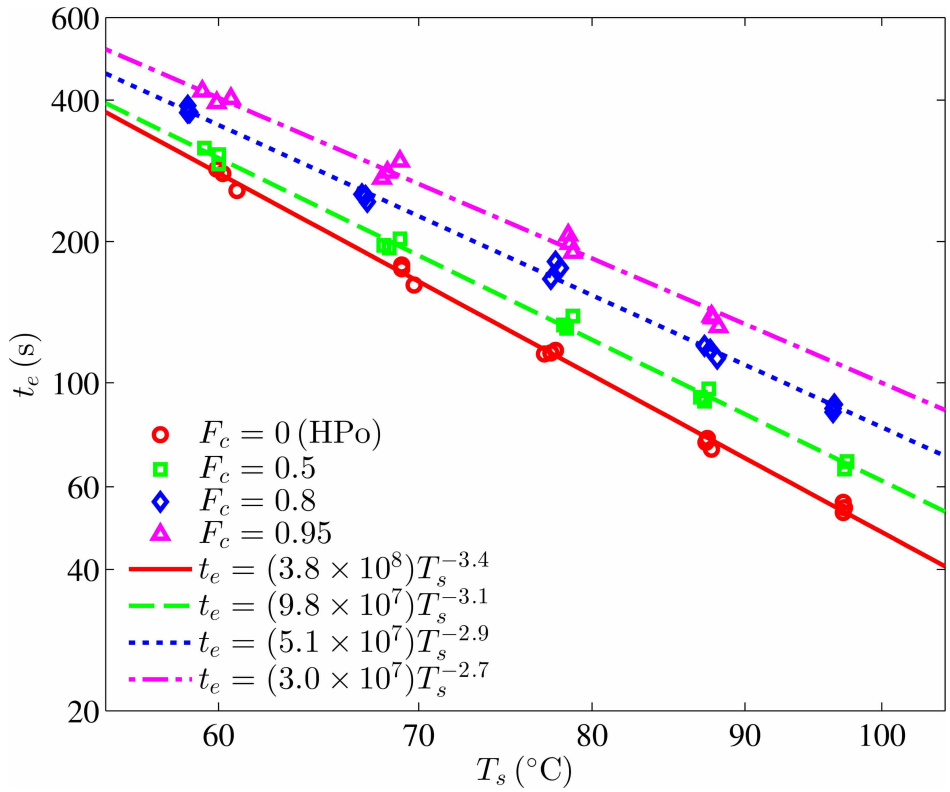

Figure 2.10: Droplet evaporation time as a function of substrate temperature for all substrates considered and for all experimental runs. Included are power-law curve fits for each substrate studied.

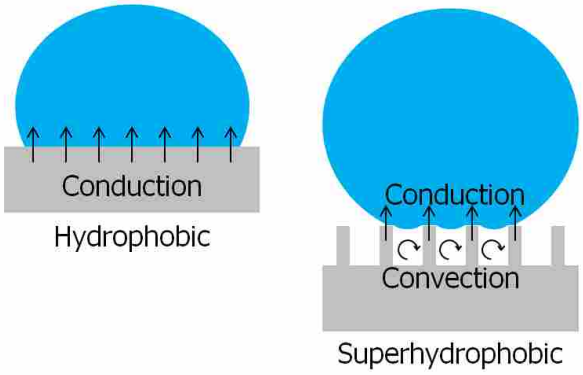

Figure 2.11: Differences in droplet-substrate interfacial heat transfer modes for SH surfaces (right) and non-SH surfaces (left).

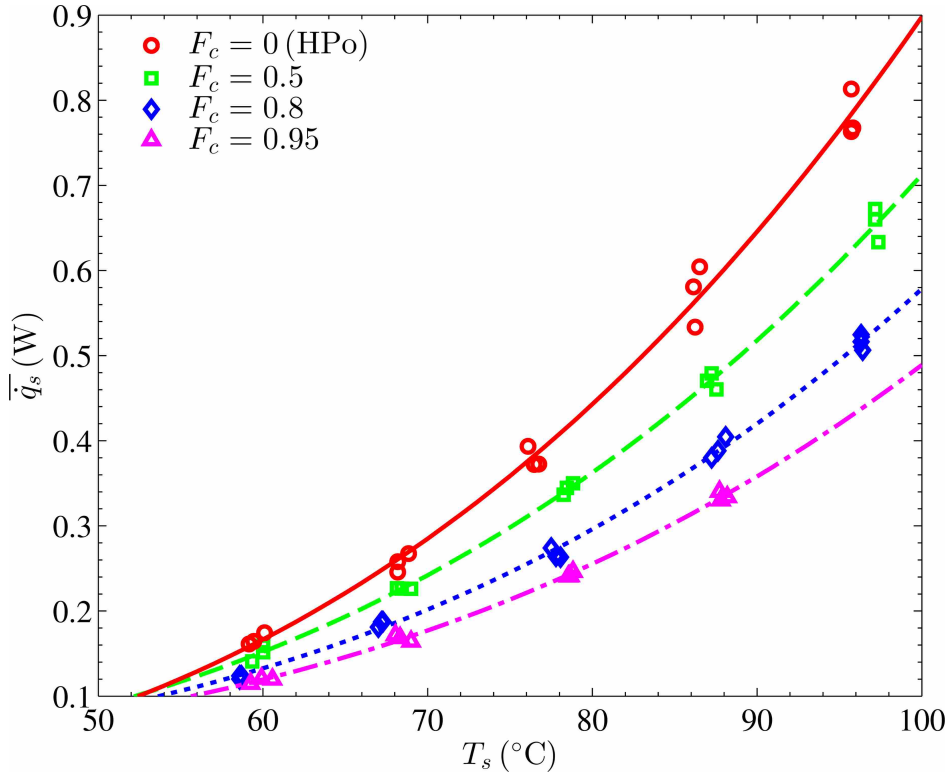

Figure 2.12: Time-averaged droplet-substrate heat transfer rate as a function of substrate temperature for all substrates studied.

A time-averaged droplet-substrate heat transfer rate, $\overline{\dot{q}_s}$, can be determined by computing $\dot{q}_s = h_{fg}\rho dV/dT$ and then averaging over time for a given substrate and T_s. Fig. (2.12) shows $\overline{\dot{q}_s}$ as a function of T_s for all substrates studied. Curves have been added to the figure to highlight the trends in the data. As T_s is increased, droplet-substrate heat transfer rates increase, as expected. Also of note is the relationship between F_c and heat transfer. As the cavity fraction is increased, heat transfer rates decrease. This explains the trends of Fig. (2.10) for evaporation times. Heat transfer rates tend to converge as T_s is decreased. This convergence can be explained by the fact that, as T_s approaches the ambient temperature, the effects of the heated surface diminish and free evaporation to the ambient air via mass transport becomes the dominant mode of heat transfer which is relatively independent of the surface type. Also of note in the figure is the repeatability of the heat transfer rate measurements. The three measurements for a given substrate type and surface temperature each fall within $\pm 4\%$ of their mean.

The average heat transfer rate, $\overline{\dot{q}_s}$, is comprised of contributions from conduction, convection, and radiation between the solid substrate and the liquid droplet. The contribution of radiation

to the overall average interfacial solid-liquid heat transfer rate can be approximated by the equation

$$\overline{\dot{q}_{s,rad}} = \varepsilon\sigma\overline{A_p}(T_s^4 - T_d^4) \tag{2.11}$$

where ε is the emissivity of the solid surface, σ is the Stefan-Boltzmann constant, $\overline{A_p}$ is the average projected area of the droplet surface that intercepts radiation from the solid surface below, T_s is the surface temperature of the solid substrate, and T_d is the temperature of the bottom surface of the droplet. If we assume the solid surface acts as a blackbody, $\varepsilon = 1$. $\overline{A_p}$ can be approximated as $\pi\overline{D_d}^2/4$, where $\overline{D_d}$ is the average horizontal diameter of the sessile droplet. In this case, $\overline{D_d} \approx 1.5\,\text{mm}$. Using the extreme case of $T_s = 100°\text{C}$ and $T_d = 70°\text{C}$, $\overline{\dot{q}_{s,rad}}$ computes to 0.5 mW, fully three orders of magnitude smaller than the contributions of conduction and convection. In reality, the emissivity of the silicon substrate is less than unity and the temperature of the droplet is much closer to the temperature of the substrate. We are justified, therefore in neglecting the contributions of radiation to the average overall interfacial heat transfer rate.

The above result holds for surfaces of high cavity fraction. Indeed, as cavity fraction approaches unity, the contribution of radiative exchange to the overall heat transfer between the solid surface and the liquid droplet remains relatively negligible in the temperature ranges studied in this thesis. If the above analysis is extended to substrate temperatures above the saturation temperature of water, and assuming T_d is equal to the saturation temperature of water, substrate temperatures in excess of 1000°C are needed to maintain radiative heat transfer rates on the same order of magnitude as those of convection and conduction.

Experiments were conducted using the infrared camera discussed earlier to determine how the droplet surface temperature varies from top to bottom. In these experiments the infrared camera viewing angle was changed from the top view used in the other experiments to a 45° isometric view and a 90° side view of the evaporating droplet. These experiments were conducted on both the smooth hydrophobic and SH surfaces. The droplet surface temperature was found to vary from hotter near the top of the droplet to cooler near the sides and bottom of the droplet. Temperature variations of about 10°C were observed. Similar variations were observed for all surface types and at all substrate temperatures studied in this paper. The presence of hotter liquid near the top of the droplet and cooler liquid near the sides of the droplet suggests the existence of buoyancy-driven, or

natural, convective cells within the droplet. These convective cells form when hot, lower density liquid near the solid surface travels upwards through the center of the droplet due to bouyant forces. As this hot liquid nears the upper surface of the droplet, it cools and increases in density, traveling downward around the sides of the droplet toward the hot surface. The results of these experiments, in combination with the results of the above analysis of radiative heat transfer, indicate that the heat transfer to the droplet is a natural convection phenomenon.

Grashof numbers, Gr, Nusselt numbers, Nu, and Prandtl numbers, Pr, were calculated for all data sets. Gr is a dimensionless number that provides a ratio between the buoyancy and viscous forces acting on a fluid. It serves as a measure of the significance of natural convection. Nu is a dimensionless ratio of convective to conductive heat transfer. It provides a measure of the significance of convection to the overall heat transfer. Pr is a dimensionless ratio of the viscous and thermal diffusivities of a fluid. It measures how quickly a fluid tends to diffuse heat relative to the speed of momentum diffusion.

The cube root of droplet volume was chosen as the characteristic length when computing Gr because this value represents the ratio between buoyant and viscous forces acting on the fluid throughout the volume of the droplet. The difference between the substrate and droplet temperatures was chosen as the characteristic temperature difference in Gr because the measured droplet temperature is the best approximation of the mean temperature of the droplet, based on experiment. This yields the equation

$$\mathrm{Gr} = \frac{g\beta(T_s - T_d)V}{\nu^2} \tag{2.12}$$

where g is the acceleration due to gravity, and β and ν are the volumetric thermal expansion coefficient and kinematic viscosity of the liquid, respectively.

The square root of the projected droplet-substrate contact area was used as the characteristic length for Nu. This value represents effective area through which convective heat transfer occurs, and we wish to characterize the heat transfer at the droplet-substrate interface. This yields the equation

$$\mathrm{Nu} = \frac{h_s A_c^{1/2}}{k} \tag{2.13}$$

where k is the thermal conductivity of the liquid.

Prandtl number is defined as

$$\mathrm{Pr} = \frac{\rho c_p \nu}{k} \tag{2.14}$$

where ρ, c_p, ν, and k are the density, specific heat capacity, kinematic viscosity, and thermal conductivity of the liquid, respectively. All fluid properties in Eqns. (2.12–2.14) were determined at the droplet temperature, T_d, and atmospheric pressure.

Fig. (2.13) shows the Nusselt number as a function of $\mathrm{Gr}^{1/4}\mathrm{Pr}^{1/3}$ for the $F_c = 0.95$ substrate case for all substrate temperatures studied. Superimposed on the data plot is a power-law curve fit of the data. This curve fit was calculated using the least squares method. Curvefits for each substrate type had similar fits and were calculated using the same method to yield

$$\mathrm{Nu}_0 = 2.53\mathrm{Gr}^{1/4}\mathrm{Pr}^{1/3} \tag{2.15}$$

$$\mathrm{Nu}_{0.5} = 2.40\mathrm{Gr}^{1/4}\mathrm{Pr}^{1/3} \tag{2.16}$$

$$\mathrm{Nu}_{0.8} = 2.14\mathrm{Gr}^{1/4}\mathrm{Pr}^{1/3} \tag{2.17}$$

$$\mathrm{Nu}_{0.95} = 1.65\mathrm{Gr}^{1/4}\mathrm{Pr}^{1/3} \tag{2.18}$$

for the $F_c = 0$, 0.5, 0.8, and 0.95 substrates, respectively.

These curves are shown graphically in Fig. (2.14). In general, Nu increases with $\mathrm{Gr}^{1/4}\mathrm{Pr}^{1/3}$ as expected. Physically, this means that as the droplet size decreases (i.e. $\mathrm{Gr} \to 0$), less heat is transferred to the drop, as shown in the discussion of Figs. (2.7) and (2.8). In addition to this general trend, for a given Gr, Nu is larger for smaller F_c. In other words, less hydrophobic substrates transfer more heat than more hydrophobic substrates. This can be explained by again looking at Fig. (2.11) and noting that as F_c is decreased (i.e. hydrophobicity is decreased) the droplet comes into greater physical contact with the substrate, leading to increased transport at the droplet-substrate interface.

Eqns. (2.16–2.18) can be normalized by dividing by Eqn. (2.15) to yield direct comparisons between Nu for each of the SH surfaces and the smooth hydrophobic surface. The results are presented in Eqns. (2.19–2.21) below.

$$\mathrm{Nu}_{0.5}/\mathrm{Nu}_0 = 0.949 \tag{2.19}$$

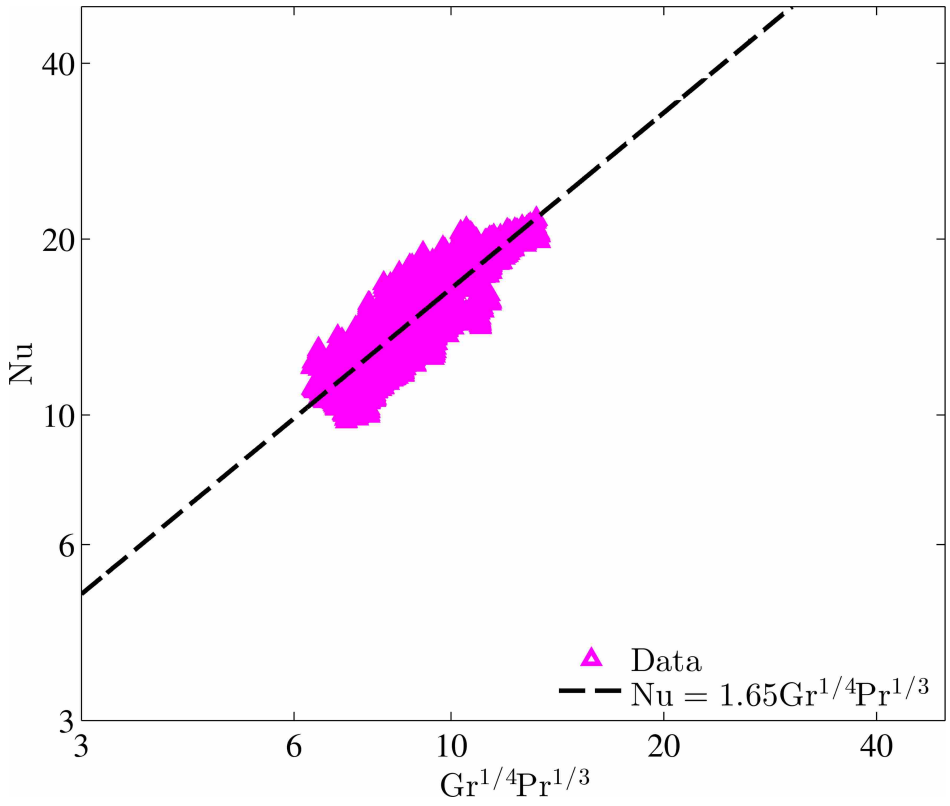

Figure 2.13: Nusselt number as a function of $\mathrm{Gr}^{1/4}\mathrm{Pr}^{1/3}$ for the $F_c = 0.95$ substrate. The experimental data is plotted along with a power-law curve fit to the data.

$$\mathrm{Nu}_{0.8}/\mathrm{Nu}_0 = 0.846 \tag{2.20}$$

$$\mathrm{Nu}_{0.95}/\mathrm{Nu}_0 = 0.652 \tag{2.21}$$

Nu decreases modestly (up to about 5%) for cavity fractions up to 0.5 but drops off dramatically as cavity fraction is increased. For a cavity fraction of 0.8, Nu is decreased by about 15% from the smoooth hydrophobic case, and for a cavity fraction of 0.95, Nu is decreased by about 35% from the smooth hydrophobic case.

Fig. (2.15) shows how the coefficient in Eqns. (2.15–2.18) relates to the solid fraction $(1 - F_c)$. Note that the power-law coefficient is about 2.5 for $0 \leq F_c \leq 0.5$. This means that there is little appreciable drop-off in heat transfer rate for cavity fractions up to about 0.5. Starting at about $F_c = 0.5$, heat transfer begins to drop off and continues to decline at an increasing rate as F_c is increased. The power-law coefficient at $F_c = 0.8$ is 2.14, for a decrease of about 15% from the smooth hydrophobic case. The power-law coefficient for $F_c = 0.95$ is 1.65, or a decrease of

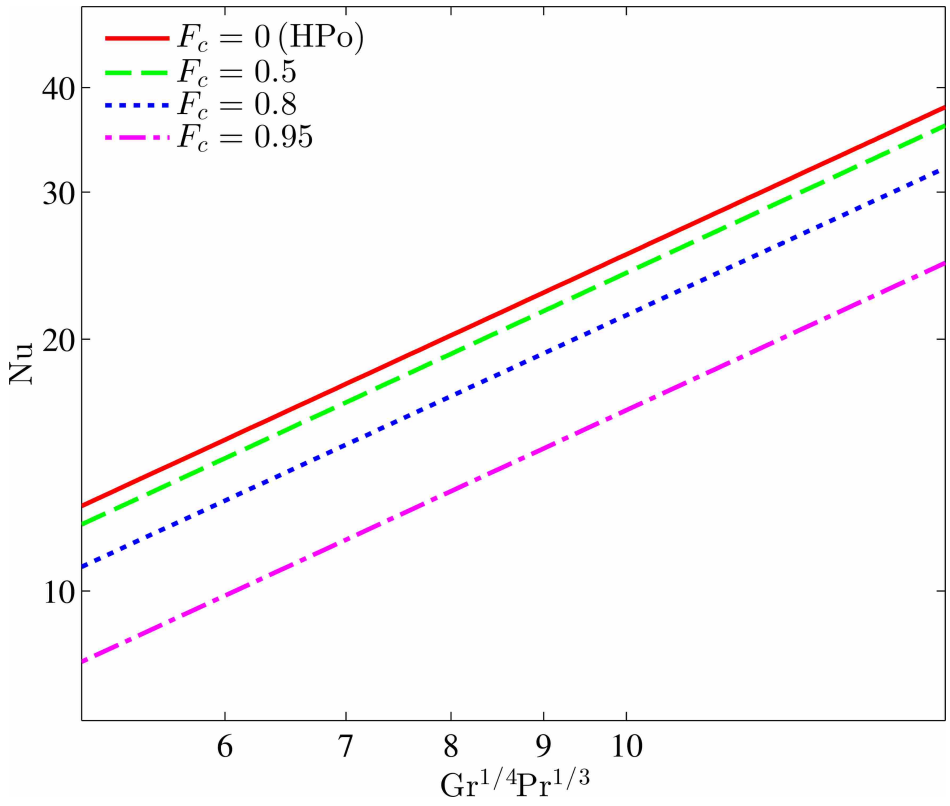

Figure 2.14: Power-law curve-fits for Nusselt number as a function Grashof number for all substrates studied.

another 20% compared to an increase in cavity fraction of only 15%. The power-law coefficient is expected to continue to decrease with even modest increases in F_c. This information is valuable for designers of products with superhydrophobic surfaces where heat transfer is of consideration in the design.

2.4 Conclusions

This paper has reported on experiments characterizing droplet-substrate heat transfer for sessile water drops resting on rib-patterned superhydrophobic substrates. At a given substrate temperature, droplet temperatures are lower for substrates with higher cavity fraction. This corresponds to increased rates of evaporation for substrates of lower cavity fraction. These trends are explained in part by the increase in contact angle that attends an increase in cavity fraction. Higher contact angles lead to lower projected droplet-substrate contact areas and, thus, an overall decrease in the amount of heat transfer. In addition, higher cavity fractions are defined by decreased phys-

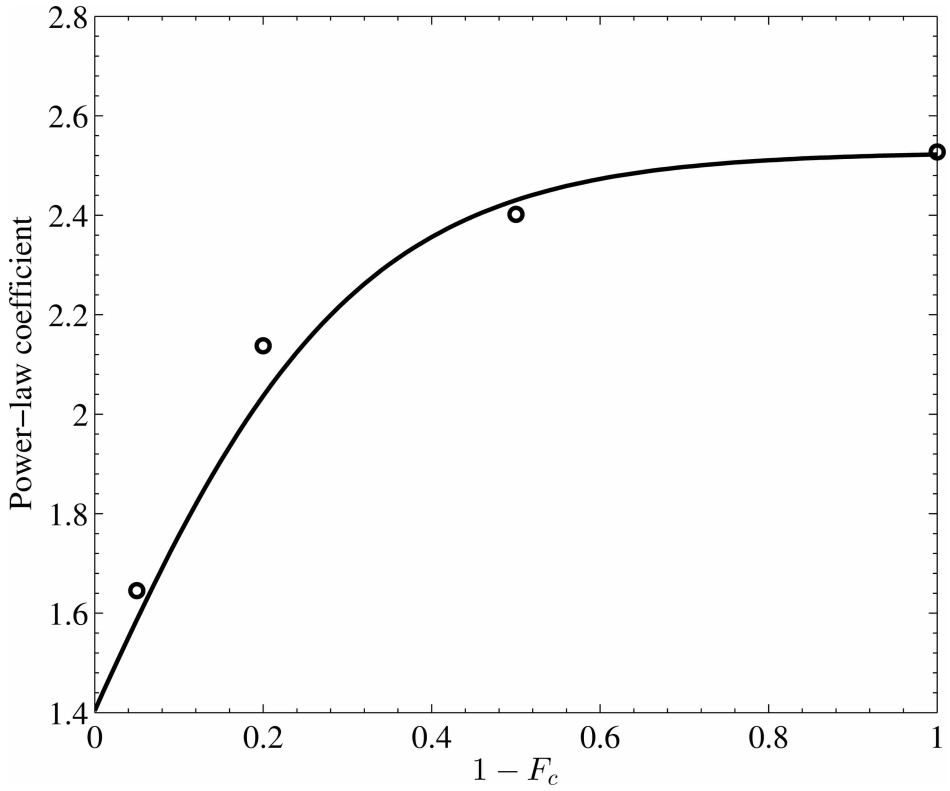

Figure 2.15: Power-law coefficient as a function of $1 - F_c$ for all substrates studied. Included is a line showing the general trend of the data.

ical contact between the droplet and the substrate, leading to a decrease in heat transfer between the droplet and the substrate.

Droplet evaporation times increase with cavity fraction as a result of the decrease in overall heat transfer. At $T_s = 60°\text{C}$, droplet evaporation time is about 300 s for the smooth hydrophobic substrate and about 400 s for the $F_c = 0.95$ substrate. At $T_s = 90°\text{C}$, evaporation time is about 80 s for the smooth substrate and about 160 s for the $F_c = 0.95$ substrate. This shows that as substrate temperature is increased, its influence on droplet-substrate heat transfer is increased.

The average droplet-substrate heat transfer rate decreases with increasing cavity fraction. Again, the difference between SH and non-SH substrates is increased with substrate temperature. At $T_s = 60°\text{C}$, $\overline{\dot{q}_s}$ is about 0.15 W for the smooth substrate and about 0.1 W for the $F_c = 0.95$ substrate. At $T_s = 90°\text{C}$, $\overline{\dot{q}_s}$ is about 0.55 W for the smooth substrate and about 0.3 W for the $F_c = 0.95$ substrate.

Plots of Nusselt number vs. Grashof number raised to the 1/4 power confirm that more heat is transferred to droplets from substrates of lower cavity fraction. For $Gr^{1/4}Pr^{1/3} = 10$, Nu is about 25 for the smooth substrate and about 15 for the $F_c = 0.95$ substrate. The trend of decreasing Nu with increasing F_c is mild for cavity fractions of between 0 and 0.5. Nu decreases more rapidly with increasing cavity fraction. Near $F_c = 0.95$, even small changes in cavity fraction exhibit appreciable changes in Nu. The data allow prediction of effective droplet-substrate heat transfer coefficients over a wide range of cavity fractions.

CHAPTER 3. THERMAL TRANSPORT TO DROPLETS AT SH SUBSTRATE TEMPERATURES ABOVE THE SATURATION POINT

3.1 Introduction

A solid surface can be classified as either hydrophobic or hydrophilic, depending on its surface energy. Higher surface energy attends a more hydrophilic surface while lower surface energy attends a more hydrophobic surface. Hydrophobic surfaces are those that exhibit internal contact angles with water in excess of 90°. Conversely, hydrophilic surfaces are those with water-solid contact angles of less than 90°. Smooth, un-textured surfaces have a theoretical upper limit on contact angle of about 120°. This limit is approached through the use of naturally hydrophobic materials such as PTFE and Teflon. Surfaces that exhibit contact angles greater than this theoretical limit can be classified as superhydrophobic (SH). This condition is made possible by the addition of microscale roughness to a hydrophobic surface. The various surface classifications are depicted in Fig. (3.1).

SH surfaces do appear in nature with examples like the lotus leaf. Such surfaces can also be manufactured artificially through a variety of methods. Nanoporous surfaces are created by distributing micropores across an otherwise smooth surface. Nanotube surfaces are created by the growth of nano-scale tubes (often made with carbon) on smooth surfaces. Nanoparticle surfaces

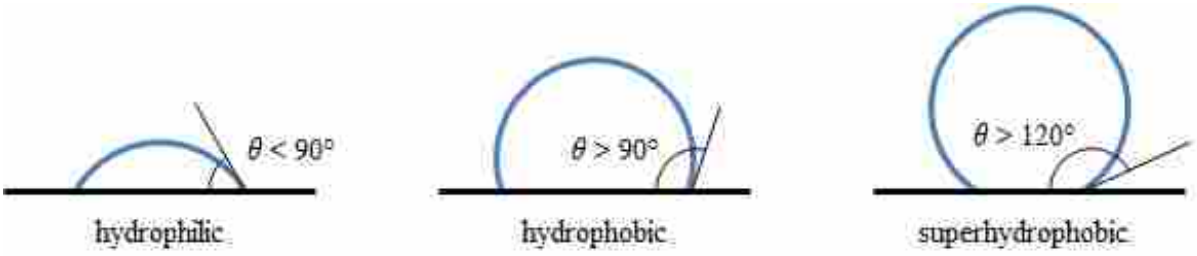

Figure 3.1: Representation of sessile droplets on surfaces of varying degrees of hydrophobicity from hydrophilic on the left to hydrophobic in the center and superhydrophobic on the right.

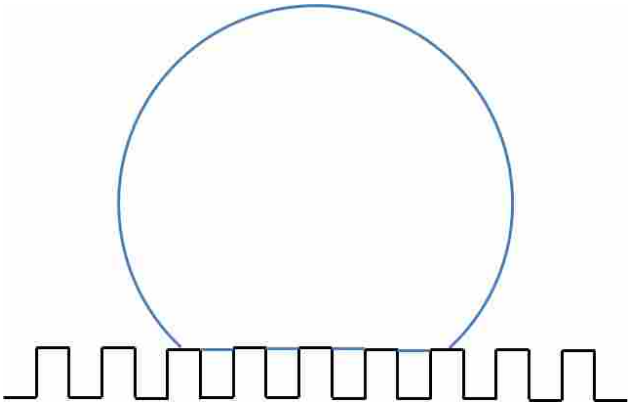

Figure 3.2: Representation of a sessile droplet in the Cassie-Baxter state on a SH surface.

are created by coating a smooth surface with a thin film of nano-disperse particles. SH surfaces created using these methods, however, have roughness that can be difficult to characterize. The random nature of the resulting surface roughness is usually disordered and difficult to characterize. Photolithography-based methods can be used to create SH surfaces with well-ordered surface roughness. These methods use masking and etching techniques similar to those used in microchip manufacture. In addition, an unlimited variety of surface patterns can be created using photolithography with ordered rows of pillars or ribs being common. The resulting roughness features are well-defined and easy to characterize.

Surface roughness enhances the hydrophobicity of a surface by creating areas of liquid-vapor interface, reducing the area of liquid-solid interface as depicted in Fig. (3.2). By reducing the overall liquid-solid contact area, the surface energy of the hydrophobic surface is minimized, increasing the contact angle of water droplets placed on the surface. This state of alternating liquid-solid, liquid-vapor contact regions is termed the Cassie-Baxter state. If the liquid pressure at the surface exceeds the Laplace pressure, liquid will flood the vapor regions and the system will enter the Wenzel state. This state is attended by a decrease in contact angle from the Cassie-Baxter state as the liquid comes into greater contact with the surface and surface energy is increased. Contact angles approaching 180° are possible on SH surfaces. In addition to liquid-solid contact angle, cavity fraction is an important parameter for SH surfaces. Cavity fraction, F_c, is defined as the ratio of projected vapor-liquid contact area to the overall projected area of the surface. Typically, an increase in F_c results in an increase in contact angle.

SH surfaces have gained recent interest in the literature for their potential application in drag reduction, lab-on-a-chip, and self-cleaning technology, among others. The heat transfer characteristics of SH surfaces are also important for many of these applications. Experiments involving pool boiling on SH surfaces were conducted by Takata et al. They found that stable film boiling occurs at even very small levels of superheat, implying the lack of a nucleate boiling regime for SH surfaces. [20]. Betz et al. included combination hydrophobic-hydrophilic surfaces, termed superbiphilic, in their study. They found that SH surfaces provided more nucleation sites for pool boiling, while superhydrophilic surfaces have higher heat transfer rates. Superbiphilic surfaces surpassed both types of surface in heat transfer efficiency by combining an increase in nucleation sites with a decrease in overall bubble size [22]. Qualitatively, their results agree well with Jo et al. [23].

Droplet heat transfer on hydrophilic and hydrophobic surfaces has been studied by many researchers. It has been shown that the evaporation rate of sessile droplets is linearly proportional to the contact radius between the droplet and the surface [31, 32]. Investigations of droplet heat transfer on SH surfaces are less common. Distinct modes of evaporation have been observed on SH surfaces depending on surface type [24, 25]. The constant contact line mode (typical of non-SH surfaces) occurs when the droplet's contact line pins to the surface and the contact angle of the droplet decreases steadily. The constant contact angle mode (typical of SH surfaces) occurs when the contact line remains unpinned and the contact angle remains constant as the contact line retreats inward. The hysteresis of a given surface is the main factor in determining which mode will dominate on a given surface [27]. Other researchers have studied the interfacial heat flux for the evaporation of sessile droplets. Smaller contact angles correlate to faster evaporation time and higher heat transfer rate [26, 32–34].

This paper seeks to characterize the drop-wise heat transfer behavior of superhydrophobic surfaces by experimentally studying the evaporation of sessile water droplets at various levels of wall superheat and for various surface patterns of ribbed SH surfaces. Evaporation times and average heat transfer rates are presented along with high-speed camera observations of deviations in boiling behavior. The effect on droplet boiling behavior of varying cavity fraction is explored. The first section outlines the experimental procedures and methods of data collection and analysis are presented. The next section presents the results of the data analysis along with observations

about the data. The final section presents conclusions about the effects of superhydrophobicity on heat transfer behavior.

3.2 Methods

Four different surface types were studied for this paper. Three of the surfaces were rib-patterened SH surfaces with varying F_c: 0.5, 0.8, and 0.95. The other surface was hydrophobic and smooth. For this paper, substrate temperatures greater than the saturation point of water were studied. At these temperatures, droplets placed on horizontal surfaces begin to translate freely, making data collection very difficult. To mitigate this problem, the smooth hydrophobic surface was constructed by forming a concave region in an aluminum plate. The radius of curvature of the concavity is very large so as to render changes in contact angle or evaporation dynamics negligible. The plate was then coated with Teflon to render the surface hydrophobic. Gravity forces keep the droplet in the center of the concavity, making data collection more feasible.

The SH surfaces were manufactured on silicon wafers using photolithography. Rib-patterns of varying F_c were laid out on silicon wafers with photoresist coatings. After development, the wafers were etched to leave the rib pattern on the surfaces. The surfaces were coated with Chromium to promote adhesion of the hydrophobic layer. The surfaces were then coated with Teflon to render them SH. The droplet translation problems present with the smooth surface are also present in the SH surfaces, but droplet boiling on SH surfaces is much less violent, reducing the need for external stabilization of the droplet. In addition, small imperfections and mineral deposits on the surface help to keep the droplet more stable by periodically pinning a small portion of the droplet to the surface, the effects of which are discussed in the results section of this paper.

Fig. (3.3) shows the various avenues for heat transfer to and from an evaporating sessile droplet. Convection, radiation, and evaporation occur between the free surface of the droplet and the surrounding medium. Conduction and convection occur between the horizontal surface and the base of the droplet. In addition, sensible heat is present in the form of droplet temperature change. Each of these heat transfer modes can be represented individually by a relatively simple equation.

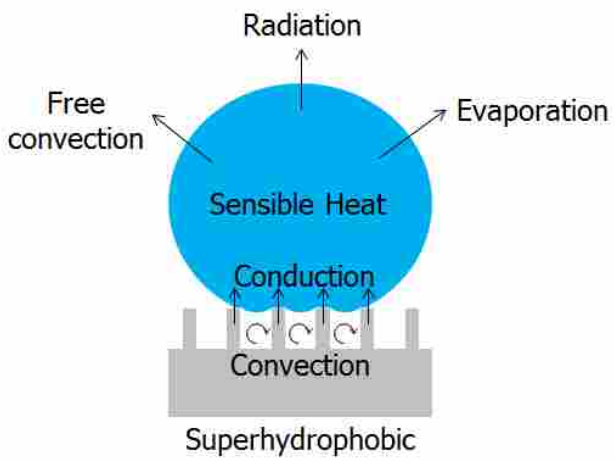

Figure 3.3: Representation of a sessile droplet on a heated SH surface with possible heat transfer modes shown.

Newton's Law of Cooling can be applied to the free convection between the free surface of the droplet and the surrounding medium to yield

$$\dot{q}_{conv} = h_{conv} A_u (T_d - T_\infty) \tag{3.1}$$

where $\dot{q}_{conv}$ is the heat transfer rate due to free convection, h_{conv} is the free convection coefficient between the droplet free surface and the surrounding medium, A_u is the surface area of the free droplet surface, T_d is the temperature of the droplet surface, and T_∞ is the temperature of the surrounding medium.

The Stefan-Boltzmann Law can be applied to the radiative exchange between the droplet and the surroundings to yield

$$\dot{q}_{rad} = \varepsilon \sigma A_u (T_d^4 - T_{surr}^4) \tag{3.2}$$

where $\dot{q}_{rad}$ is the heat transfer rate due to radiation between the droplet and the surroundings, ε is the emissivity of the droplet free surface, σ is the Stefan-Boltzmann constant, and T_{surr} is the temperature of the surroundings.

Evaporation can be modeled by

$$\dot{q}_{evap} = h_{fg} \rho \frac{dV}{dt} \tag{3.3}$$

where $\dot{q}_{evap}$ is the heat transfer rate due to evaporation, h_{fg} is the latent heat of vaporization of the droplet liquid, ρ is the density of the droplet liquid, and dV/dt is the time rate of change of droplet volume.

Sensible heat change within the droplet can be modeled by

$$\dot{q}_{sens} = c_p \rho V \frac{dT_d}{dt} \tag{3.4}$$

where $\dot{q}_{sens}$ is the energy storage rate due to sensible heat, c_p is the specific heat capacity of the droplet liquid, V is the droplet volume, and dT_d/dt is the time rate of change of droplet temperature.

It has been shown by the current authors that the only non-neglible heat loss for a sessile droplet in free evaporation is that due to evaporative cooling [37]. The heat transfer to the droplet from the surface, $\dot{q}_s$, can therefore be accurately modeled by

$$\dot{q}_s = \dot{q}_{evap} = h_{fg} \rho \frac{dV}{dt} \tag{3.5}$$

An experiment was designed to capture the relevant variables for Eqns. (3.1–3.4). The overall experimental setup is shown in Fig. (3.4). The test surfaces are placed horizontally on an insulated, heated aluminum block. The heat input to the block is controlled by a voltage transformer, and the temperature of the block is monitored using a K-type thermocouple which is embedded approximately 3 mm below the top surface of the block. Distilled water droplets are placed on the test surface using a glass syringe with a Teflon needle. Glass and Teflon are used because particulate contamination from metals can cause droplets to prematurely pin to the surface during evaporation. An infrared camera placed directly above the test surface measures the droplet temperature at the top of the droplet. Two CCD cameras are placed perpendicular to one another and normal to the sides of the droplet. These gather geometric data from the droplet such as volume and contact area. Both sets of cameras are connected to computers with video capture hardware and software onboard. A combination thermometer and hygrometer measures the ambient air temperature and relative humidity.

Experiments were performed by heating the block to various steady-state temperatures above the saturation point of water from 100 to 230°C. A single sessile droplet of distilled water is then placed on the surface. The cameras capture temperature and geometry data as the droplet

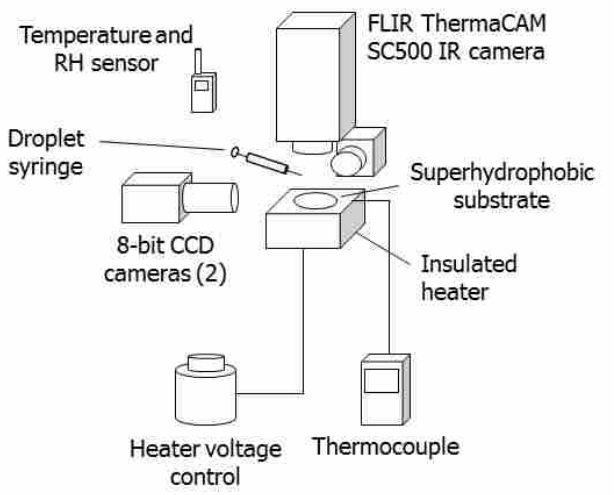

Figure 3.4: Experimental setup used for gathering data.

evaporates. Measurements of ambient air temperature and relative humidity are also recorded. Three trials were recorded at each surface temperature and for each surface type.

The CCD camera images were post-processed in MATLAB using algorithms written by the author for the purpose. The droplet images first need to be segmented to distinguish the droplet from the rest of the image. This is accomplished by applying a grayscale intensity thresholding argument. This produces a binary image where the background becomes black and darker objects (such as the droplet outline) become white. Noise, particles, and other unwanted image artifacts are discarded from the images and the final shape of the droplet is reproduced by creating a convex hull around the droplet outline found in the previous steps. The results of these operations are presented in Fig. (3.5).

The binary representations of the droplet shape are further processed to produce measurements of droplet geometry. After calibrating the camera setup with a known geometry, a conversion between pixel counts and physical units of length can be found. Droplet volume is found by first calculating the horizontal distance in number of pixels between the left and right edges of a droplet at a given row of pixels. This pixel distance is converted to physical units to produce the droplet diameter at a given vertical location. The volume of a single-pixel-thick volume-element disk is given by the equation

$$V_i = \frac{\pi d_i^2 h_p}{6} \tag{3.6}$$

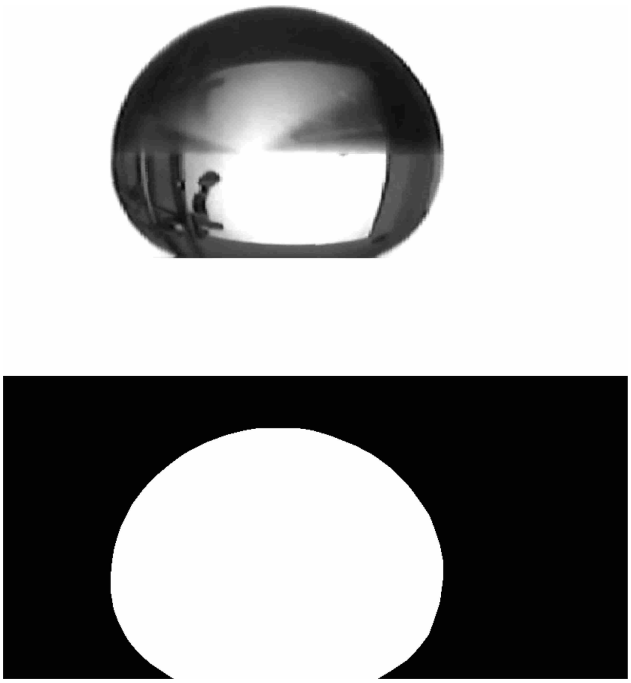

Figure 3.5: CCD image of a droplet resting on the $F_c = 0.95$ substrate (top) and the binary transformation of this image after processing (bottom).

where V_i is the volume of the volume-element disk, d_i is the diameter of the volume-element disk, and h_p is the width of a single pixel in physical units. The volumes can be summed over all vertical locations, i, to produce an approximation of the volume of the droplet. The volumes as approximated by the images from each camera angle can be averaged to produce an even more accurate approximation of the droplet volume.

High speed video images of the droplet were also captured by replacing the CCD cameras with a single high speed video camera. Video was captured at 10000 FPS. The high-speed footage was not post-processed to produce quantitative data, but instead was reviewed for qualitative observations of the process of droplet evaporation.

3.3 Results

Volume data obtained for droplets in the nucleate and transitional boiling regimes tends to be very noisy due to rapid droplet oscillations. Finding dV/dt for Eqn. (3.5) necessitates smoothing of the volume data. For this paper, the volume data were smoothed with a weighted, 3rd degree polynomial, linear least squares regression. In addition, irrespective of initial droplet volume, the

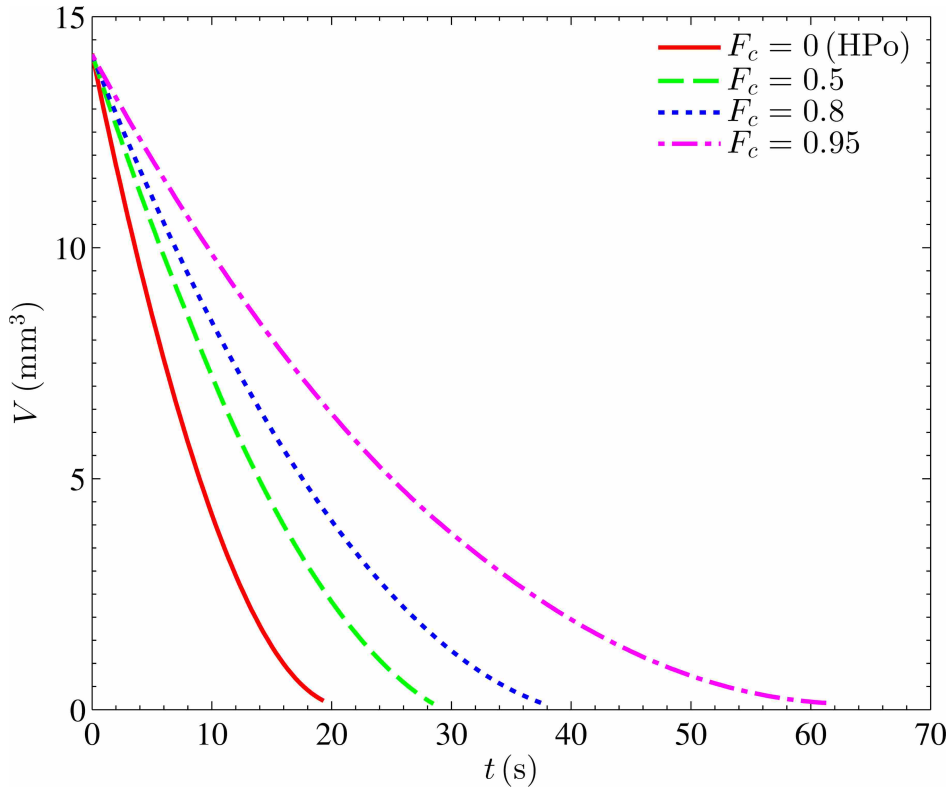

Figure 3.6: Droplet volume through time for all surface types at $T_s = 160°\mathrm{C}$.

volume data processing began at a droplet diameter of 3 mm to ensure consistency of measurement in making direct comparisons. Fig. (3.6) shows some examples of transient volume data for each surface type studied at a substrate temperature of $T_s = 120°\mathrm{C}$. In general, the droplet volume data show a decreasing slope with increasing F_c. This corresponds to a decrease in evaporation rate with increasing F_c.

Differences in evaporation rate are again reflected in measurements of droplet evaporation time, t_e. Fig. (3.7) shows droplet evaporation times for each surface type and temperature studied. Included are the evaporation time data for temperatures below the saturation point of water from Hays et al. [37] At surface temperatures, T_s, below the saturation point of water, evaporation time decreases with decreasing F_c. Furthermore, as T_s is increased, t_e decreases. This is expected, as higher heat inputs should yield higher evaporation rates and lower evaporation times. Each surface type appears to have a minimum in t_e at around $T_s = 130°\mathrm{C}$. This minimum in t_e corresponds to the critical heat flux (CHF) point where heat input reaches a maximum. From this point on, the distinciton in t_e between the hydrophobic and SH surfaces becomes less clear. Evaporation time

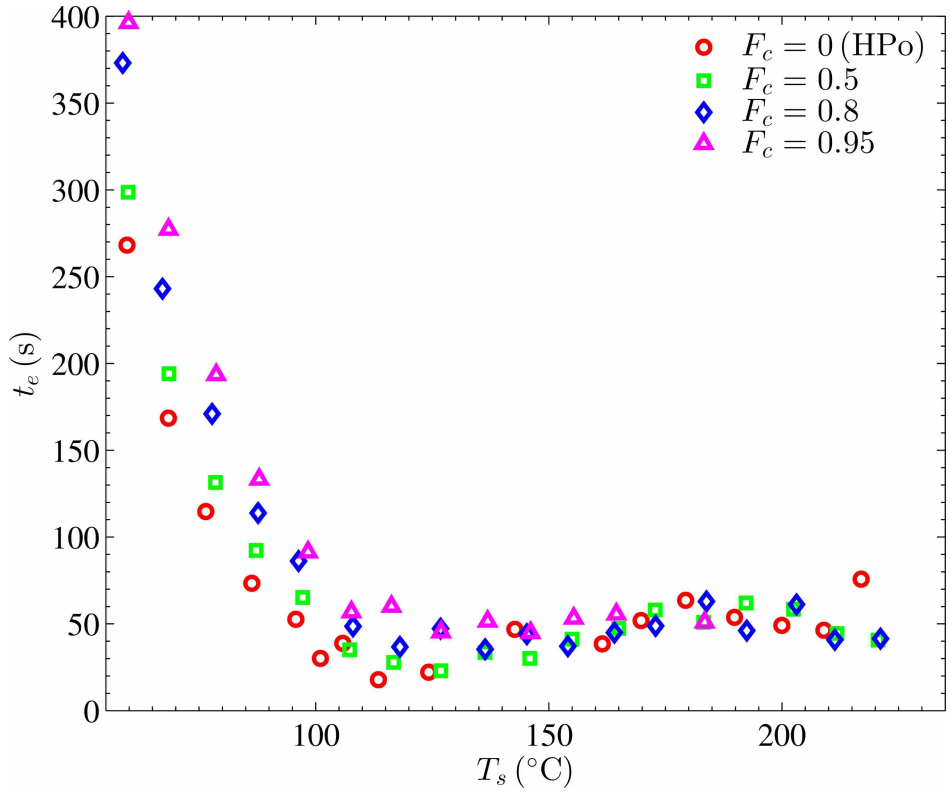

Figure 3.7: Droplet evaporation times for all surface types and temperatures studied.

increases slightly as T_s is increased beyond 130°C. This corresponds to the transition between nucleate boiling and film boiling. Heat is transferred more efficiently via nucleate boiling as more liquid is in contact with the solid surface than for film boiling where an insulating vapor film forms at the solid surface. This decrease in heat transfer leads to slightly increased evaporation times as shown.

An examination of the droplet heat loss due to evaporation sheds further light on the differences in boiling phenomena between the various surfaces. The volume data are used to compute dV/dt in Eqn. (3.5). In this manner, the value of $\dot{q}_s$ at any point in the droplet's lifetime can be estimated. Droplet pinning begins to have an effect on evaporation dynamics near the end of the droplet's life, so $\dot{q}_s$ is averaged over a subset of the total time domain shown in Fig. (3.6). It was observed that the droplet never pins before at least 90% of the droplet's volume has evaporated. To yield consistent results, $\dot{q}_s$ is averaged over the time domain corresponding to $V_0 \geq V \geq 0.1V_0$, where V_0 corresponds to droplet volume at $t = 0$ in Fig. (3.6). This yields an average heat input, $\overline{\dot{q}_s}$. Fig. (3.8) shows the average heat input plotted against the surface superheat, $T_s - T_{sat}$. Curves

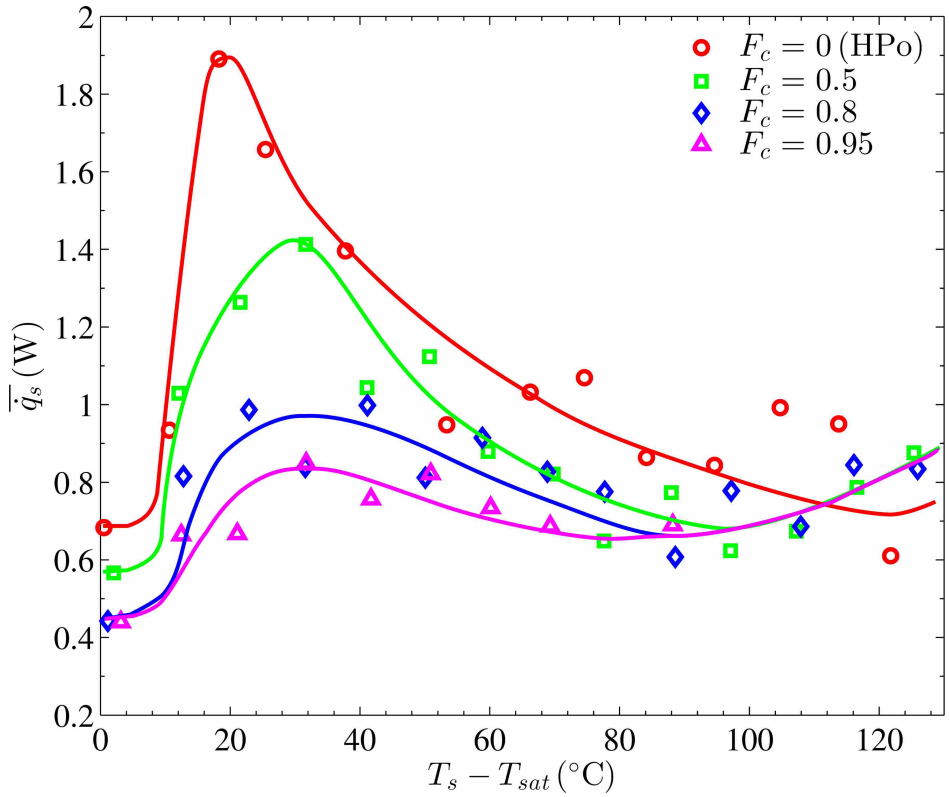

Figure 3.8: Average heat transfer rate vs. superheat for all surface types and temperatures studied.

have been added to the plot to show the trends in the data more clearly. This plot can be compared with the classical boiling curve for saturated water with good qualitative agreement.

The general trend in the curves of Fig. (3.8) is similar across all F_c. The average heat input increases with superheat until it reaches a maximum near 30°C of superheat. Average heat input then decreases steadily until it reaches a minimum near 100°C of superheat, though this minimum occurs at lower superheats for higher F_c. Average heat input then begins to increase slowly. As F_c is increased, average heat input decreases at a given superheat. The average heat input curve also flattens as F_c is increased yielding lower maximum average heat inputs for higher F_c.

For the smooth hydrophobic surface (open circles in Fig. (3.8)), maximum heat input occurs at a superheat of about 20–30°C. This corresponds well to the critical heat flux point in the classical boiling curve for smooth surfaces. The Leidenfrost point, corresponding to a minimum in heat input, occurs at about 120°C for smooth surfaces in the classical boiling curve. The limitations of the experimental setup didn't allow for superheats greater than about 120°C, but the data do appear

to be approaching a minimum value for the smooth surface, and the last data point at about 120°C of superheat is lower than those proceeding it.

The SH surfaces show different behavior depending on F_c. For the $F_c = 0.5$ surface, a maximum occurs at about 30°C of superheat, though the heat input is about 1.4 W compared to about 1.9 W for the smooth surface. A minimum in heat loss, corresponding to the Leidenfrost point, occurs at about 100°C of superheat.

For the $F_c = 0.8$ SH surface, behavior begins to depart from the classical boiling curve. Though a maximum in heat input again occurs at about 30°C of superheat, the maximum is less distinguishable from the succeeding data points. The Leidenfrost point is also less distinguishable than for the $F_c = 0.5$ case, but seems to occur at about 90°C of superheat. This is slightly less superheat than for the $F_c = 0.5$ case.

The behavior of the $F_c = 0.95$ SH surface departs even further from classical boiling behavior. Here, there the critical heat flux point seems to be almost indistinguishable from the Leidenfrost point, though the heat transfer rate, $\overline{\dot{q}_s}$, does seem to reach a maximum at about 30°C of superheat, as before. At superheats of greater than about 90°C, data collection was impossible for this surface as the droplets translated freely on the surface.

High-speed video was captured at various superheats for all substrates studied. The videos provide visual evidence of the decrease in heat transfer with increasing cavity fraction. Fig. (3.9) shows a series of frames from each substrate at $T_s - T_{sat} \approx 30$°C. The frames shown were sampled from the high speed videos at 0.0005 s intervals. The top row of images show a droplet evaporating on the smooth hydrophobic surface. Of note in this set of images is the presence of rapid droplet surface agitation, indicative of nucleate boiling. The second row shows a droplet on the $F_c = 0.5$ surface. Note the marked decrease in surface agitation indicative of a decrease in heat transfer from this substrate. The third row of Fig. (3.9) shows a droplet evaporating on the $F_c = 0.8$ surface. Nucleate boiling is notably absent in this set of images, though a small degree of surface agitation is still present. The bottom row of images shows a droplet evaporating on the $F_c = 0.95$ surface. No surface agitation is present in these images, indicating a tremendous reduction in heat transfer from the smooth and lower cavity fraction cases.

Fig. (3.10) shows high speed images of droplet evaporation at a range of substrate temperatures for the smooth hydrophobic surface. As in the previous figure, frames were sampled at

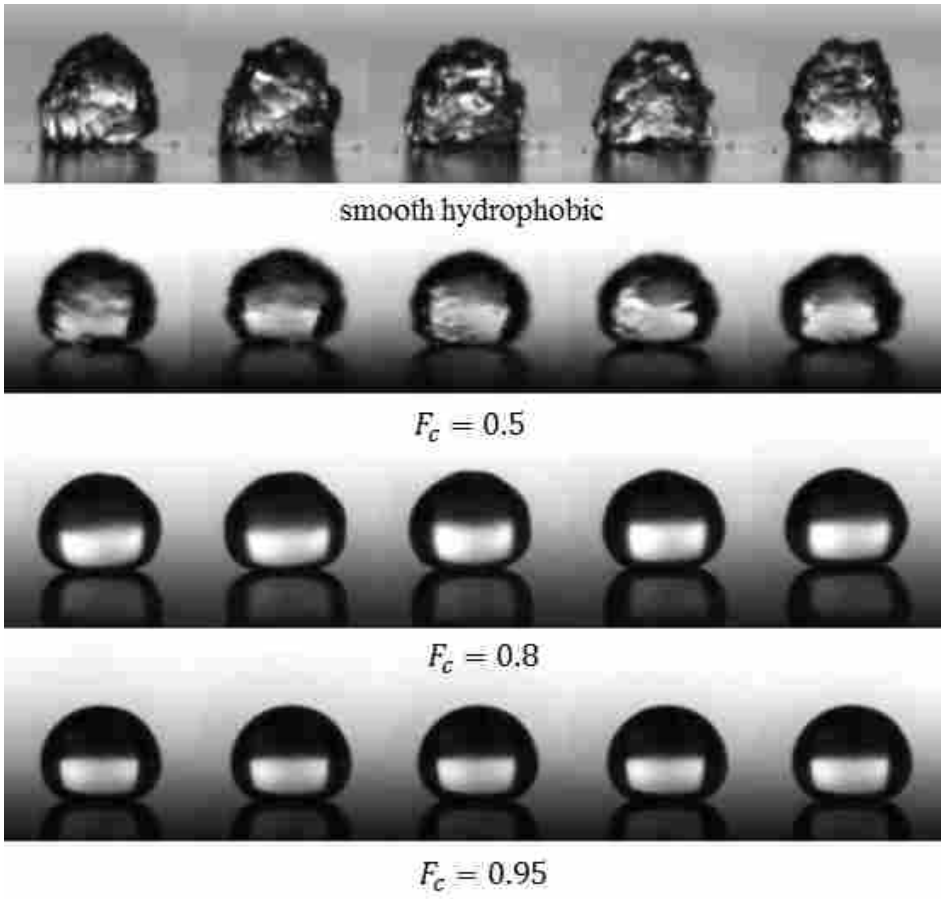

Figure 3.9: High speed images of droplet evaporation at $T_s - T_{sat} \approx 30°C$. Images were taken at 0.0005 s intervals. Each row is from a different substrate type: smooth hydrophobic (top), $F_c = 0.5$ (second), $F_c = 0.8$ (third), and $F_c = 0.95$ (bottom).

0.0005 s intervals. In the top row, the surface is at approximately 85°C or 10°C below the saturation point of water. Boiling is notably absent, as expected. The second row shows the surface at approximately 10°C of superheat. This is near the onset of nucleate boiling, and the droplet shows signs of boiling with observable surface agitation. In the third row of images, the surface is at approximately 30°C of superheat, near the critical heat flux temperature. The surface agitation is most pronounced in this set of images, lending support to the quantitative maximum in heat transfer rate near this substrate temperature. The last three rows show the surface at increasing substrate temperatures. Notably, the surface agitation is lessened with increasing superheat. As the droplet nears the Leidenfrost point at approximately 120°C, these surface agitations are expected to die out completely as a stable vapor layer forms and nucleate boiling ends.

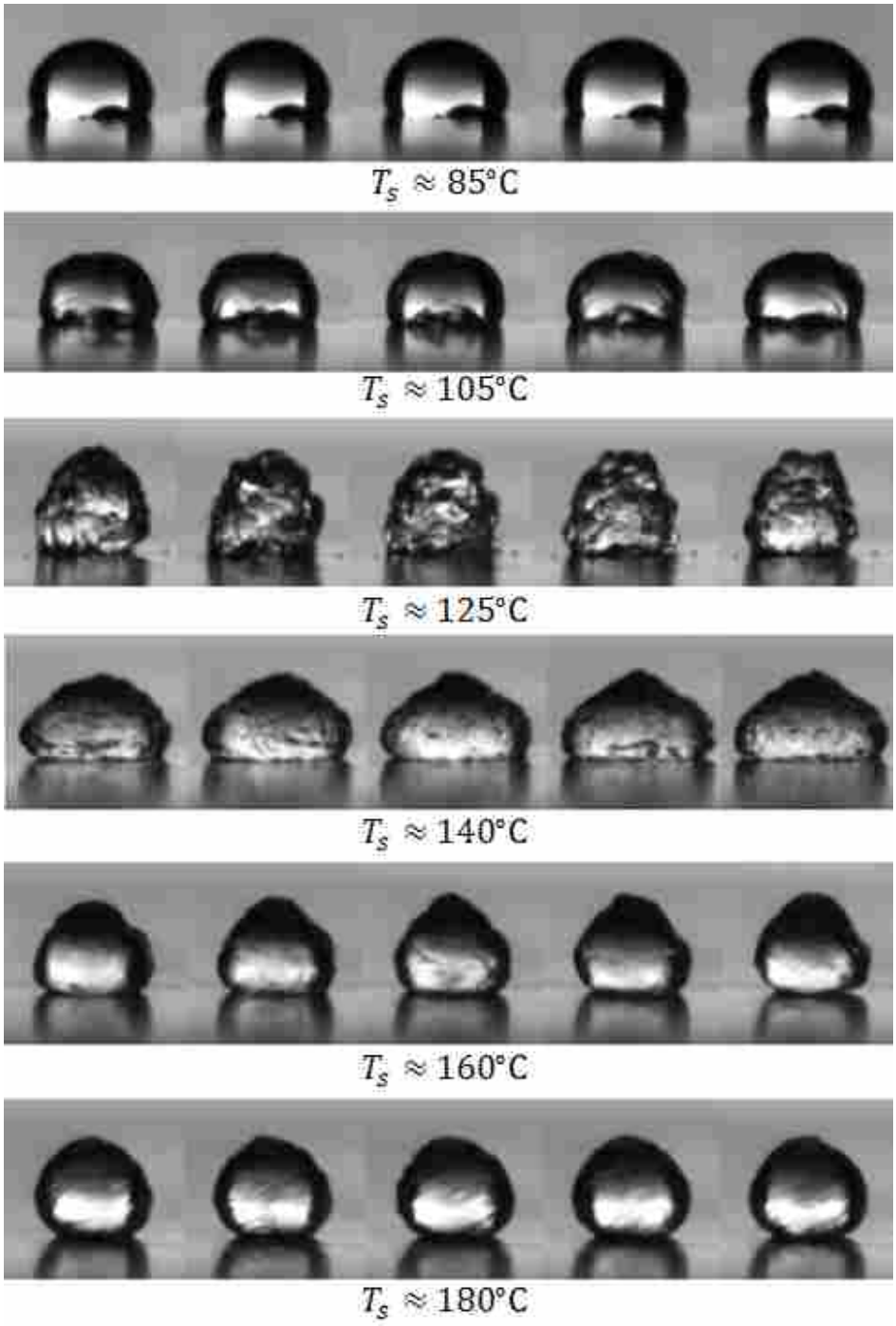

Figure 3.10: High speed images of droplet evaporation on the smooth hydrophobic surface at various superheats. Images were taken at 0.0005 s intervals. Each row is from a different substrate temperature, as noted.

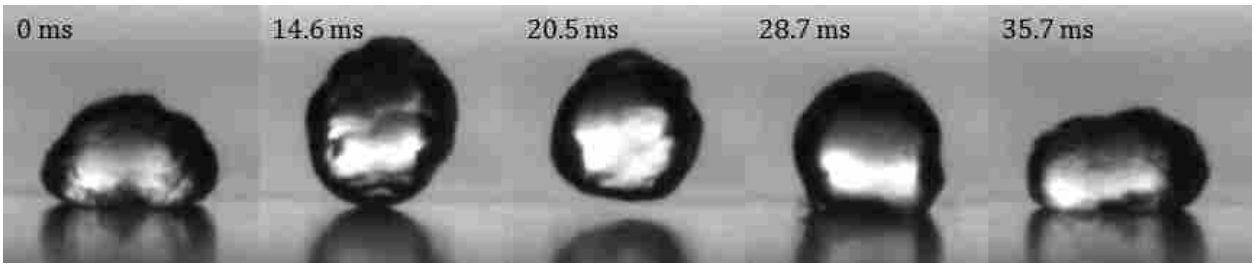

Figure 3.11: The bouncing droplet phenomenon as observed in high speed images of droplet evaporation at $T_s - T_{sat} \approx 170°C$ on the smooth hydrophobic surface. Time stamp relative to first image is included in top-left of each image.

Fig. (3.11) shows an example of a bouncing droplet phenomenon that occurs on the smooth hydrophobic surface at certain superheat temperatures in the transition region between the critical heat flux point and the Leidenfrost point. As the droplet is heated by the solid surface, a strong convective current forms in the droplet creating a jet that propels the droplet upward. The droplet leaves the surface and begins to cool before falling back down to the heated surface. This unstable heating and cooling cycle continues, causing the droplet to oscillate for most of the evaporation process. As substrate temperature is increased to the Leidenfrost point, these oscillations die out as a stable vapor film is formed beneath the droplet.

The high-speed images shed further light on the phenomena at work in the preceeding heat input plots. Fig. (3.12) shows the average heat input data for the smooth surface only. The accompanying images are frames from high speed video of droplet evaporation on a smooth surface at various levels of superheat. The images are placed at their appropriate location on the x-axis. The first image from the left is placed in the region where nucleate boiling occurs. Vapor bubble formation can be seen at the base of the droplet and the outer surface of the droplet is unstable due to the escape of vapor to the outside air. The second image is near the critical heat flux point. Vapor bubbles are present throughout the droplet and the surface of the droplet is very agitated as rapid boiling occurs. The third image is from the transition boiling region. Here, the droplet oscillates up and down on an intermittent vapor layer as it transitions from nucleate to film boiling. The last image is near the Leidenfrost point. The surface of the droplet is remarkably less agitated, and oscillations have almost ceased. The droplet does continue to oscillate near the end of its life, as shown by the images of the smaller droplets, but almost no agitation of the surface is observed, suggesting the presence of film boiling alone.

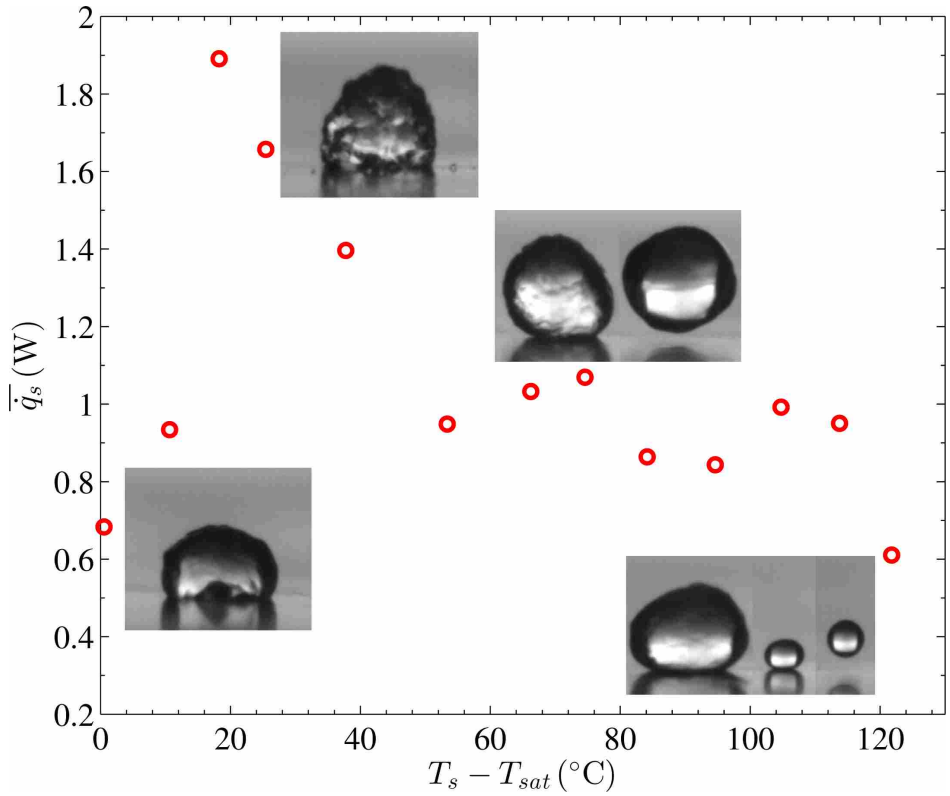

Figure 3.12: Average heat transfer rate vs. superheat for the smooth surface with high speed images included for comparison.

Fig. (3.13) shows the average heat input data for the $F_c = 0.5$ SH surface. The first image shows how the SH surfaces lead to a delay in the onset of nucleate boiling. The first image of Fig. (3.13) and Fig. (3.12) was taken at the same superheat. The droplet on the SH surface shows no observable surface agitation or bubble formation. Much nearer to the critical heat flux, in the second image, the droplet shows full agitation, though to a lesser degree than for the smooth surface. In the transition boiling regime, image three shows the droplet resting on an unstable vapor film. While there is no droplet oscillation, the droplet takes on a deformed, elongated shape. The last image shows the droplet in the Leidenfrost state. No oscillation or agitation of any kind is visible and the droplet is now at a much higher contact angle than in the first image.

The same plot is shown for the $F_c = 0.8$ SH surface in Fig. (3.14). Here, we see the same delay in the onset of nucleate boiling as for the lower cavity fraction surface in the first image. Again, the droplet is much less agitated, even less than the $F_c = 0.5$ surface, at the crtical heat flux point in the second image and in the transition region in the third image. The last image again

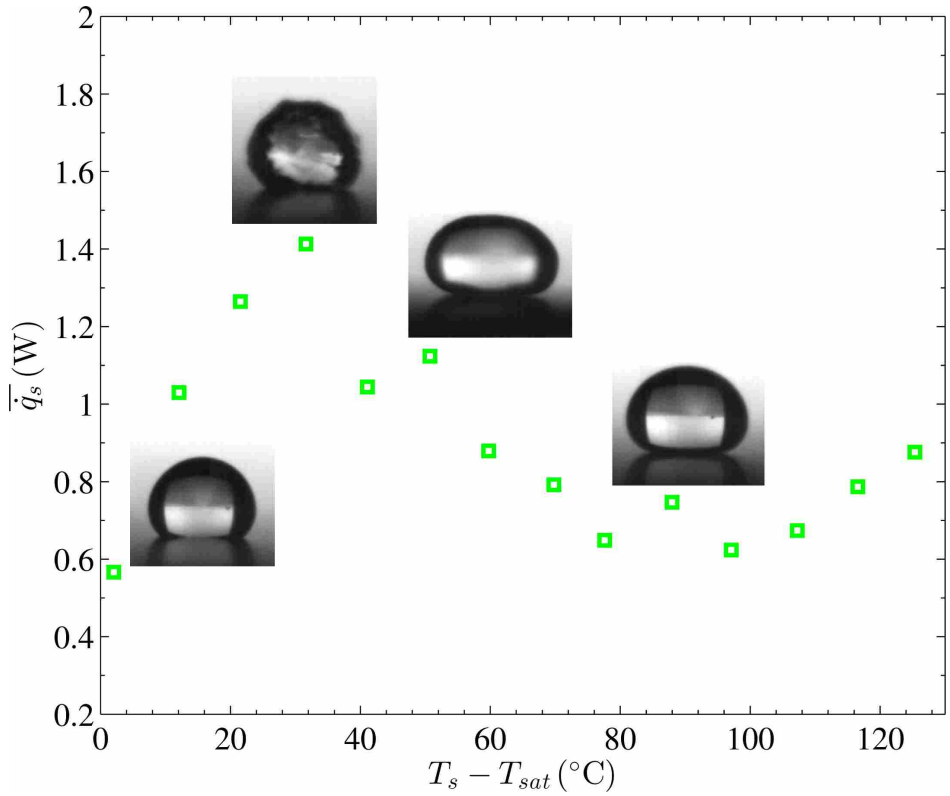

Figure 3.13: Average heat transfer rate vs. superheat for the $F_c = 0.5$ surface with high speed images included for comparison.

shows the droplet at the Leidenfrost point. Here, however, the contact angle is only slightly greater than for the first image, in contrast to the larger disparity in Fig. (3.13).

Images in Fig. (3.15) depict the same processes for the $F_c = 0.95$ surface. The high speed images taken never captured any observable surface agitation, suggesting that nucleate boiling is never observed for the $F_c = 0.95$ surface. In addition, it would appear that the Leidenfrost point occurs much earlier than for the other surfaces, possibly even being coincident with the critical heat flux point.

The gradual flattening of the curves with increasing F_c shown in Fig. (3.8) can now be explained in terms of the variation in liquid-solid contact area between surfaces. As F_c is increased, less of the solid surface comes into contact with the droplet and, conversely, the droplet comes into greater contact with vapor. As vapor is a poorer conducter of heat, this leads to a decrease in the overall heat input to the droplet. The result is lower maximum heat inputs and lower heat inputs overall at any given superheat for higher F_c.

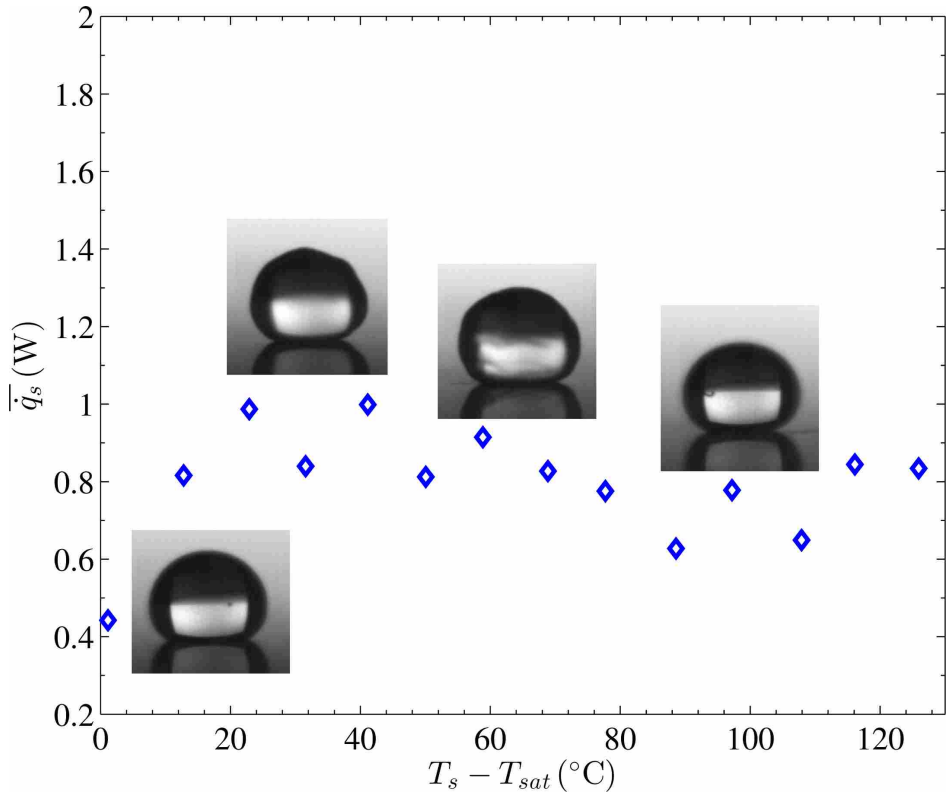

Figure 3.14: Average heat transfer rate vs. superheat for the $F_c = 0.8$ surface with high speed images included for comparison.

The increase in liquid-vapor contact at higher F_c also leads to a decrease in the superheat at which Leidenfrost behavior occurs. Because the droplet is already partially supported by a vapor layer in the cavities of the surface features, less superheat is required to create a stable film layer that supports the entire droplet. Interestingly, as superheat is increased beyond the Leidenfrost point, the average heat input for all F_c seems to collapse to a single curve.

The intermittent droplet pinning required for data collection on the SH surfaces leads to some variation in the data. Fig. (3.8) shows that average heat inputs can vary by up to about 10% depending on the pinning dynamics for a particular droplet evaporation event, though some of the variation can probably be mitigated by increasing the number of tests at a given substrate temperature.

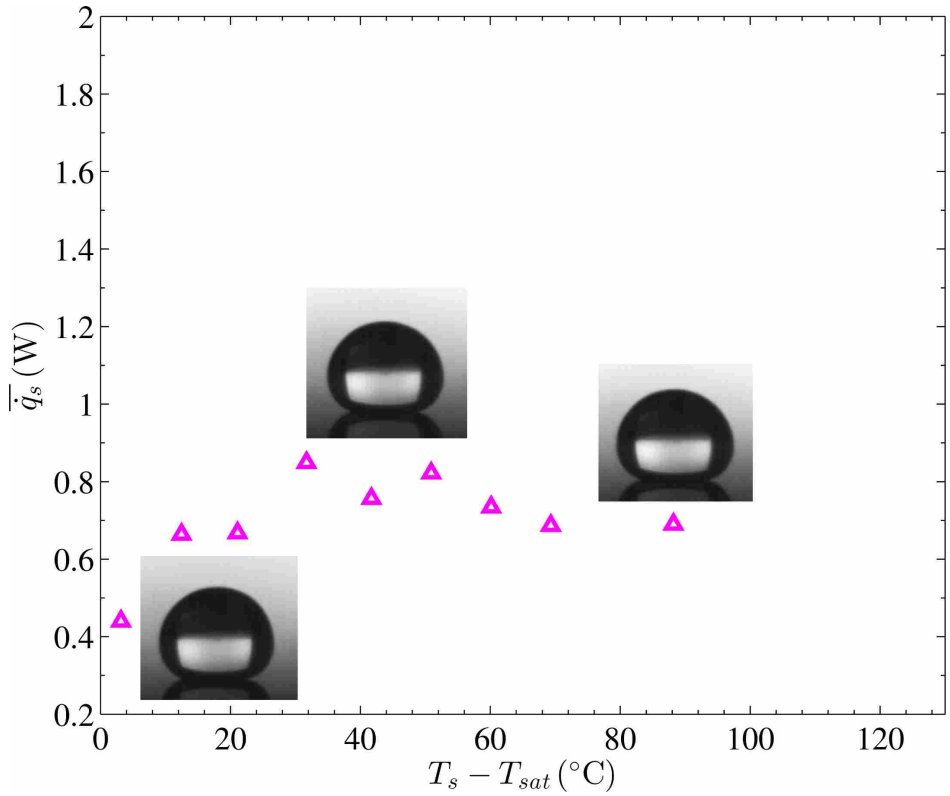

Figure 3.15: Average heat transfer rate vs. superheat for the $F_c = 0.95$ surface with high speed images included for comparison.

3.4 Conclusions

Increasing the cavity fraction of a surface decreases the heat input to a droplet placed on the surface at superheats below the Leidenfrost point. As the Leidenfrost point is reached, similar heat inputs are observed for all surface types.

Increasing the cavity fraction of a SH surface also delays the onset of nucleate boiling and decreases the superheat at which Leidenfrost behavior occurs. If the cavity fraction is increased enough ($F_c = 0.95$ for this paper), nucleate boiling is never observed and the droplet exhibits Leidenfrost-like behavior at about the critical heat flux point.

The Leidenfrost point for 3 mm diameter sessile water droplets occurs at approximately 100°C of superheat for $F_c = 0.5$ and $F_c = 0.8$ surfaces. The Leidenfrost point for the $F_c = 0.95$ surface is much lower at about 30°C of superheat. This change in Leidenfrost behavior can be explained by the presence of persistent vapor cavities on the SH surfaces. These cavities act to stabilize the vapor film beneath the boiling droplet at lower superheats.

The delay in nucleate boiling can also be explained by the presence of the vapor cavities. Heat is conducted much more poorly through vapor than it is through the solid surface. This leads to an overall decrease in heat transfer from the surface to the droplet, thus delaying the onset of nucleate boiling.

CHAPTER 4. CONCLUSION

4.1 Summary

Cavity fraction, F_c, is an important parameter in characterizing the heat transfer for SH surfaces. As F_c is increased, overall heat transfer rates to sessile droplets decrease. This overall trend is observed both above and below the saturation point of water. At substrate temperatures below the saturation point, droplet evaporation times decreasely monotonically with increasing substrate temperature. At a given substrate temperature, evaporation times increase with increasing F_c. Also, at a given substrate temperature, droplet temperatures decrease with increasing F_c. Nu also decreases with increasing F_c. For $0 \lesssim F_c \lesssim 0.5$, Nu decreases mildly with increasing F_c. As F_c approaches unity, Nu decreases much more dramatically with increasing F_c.

The effects of decreased heat transfer are also apparent at temperatures above the saturation point of water. Differences in droplet evaporation time are much less pronounced at superheat substrate temperatures than at temperatures below the saturation point. Nucleate boiling is delayed to higher superheats compared to smooth surfaces at lower F_c ($0 < F_c \lesssim 0.8$), and completely disappears at higher F_c ($\gtrsim 0.8$). In addition, the Leidenfrost point occurs at lower superheats as F_c is increased. This points to the fact that SH surfaces more readily enter the film boiling regime compared to smooth surfaces. At superheats above the Leidenfrost point, SH surfaces exhibit similar heat transfer rates.

These changes in heat transfer and boiling behaviorn with F_c can be explained by the change in solid-liquid contact area. As F_c is increased from 0, the droplet comes into greater contact with vapor trapped in the cavities of the surface. As vapor is a much poorer conductor of heat compared to solid silicon, this leads to a decrease in heat transfer rate with increasing F_c. The vapor cavities have the added effect of delaying the onset of nucleate boiling to higher superheats compared to smooth surfaces, due to the decrease in heat input. The presence of vapor cavities

in SH surfaces also acts to promote the formation of a stable vapor film beneath the droplet. This explains the decrease in the superheat required for Leidenfrost behavior.

4.2 Further work

The limitations of the current experimental setup didn't allow for superheats above 120°C. The material used for insulation of the heater block is susceptible to burning at higher temperatures. Additionally, droplets placed on SH surfaces above this temperature readily translate off the surface, making data collection impossible. Unfortunately, this is precisely the Leidenfrost point for smooth surfaces. As the SH surfaces appear to exhibit similar heat transfer rates at superheats beyond their respective Leidenfrost points, it would be interesting to see if smooth surfaces and SH surfaces have similar heat transfer rates at superheats above 120°C.

The current research did not fully investigate the nucleate boiling regime between 0 and 30 °C of superheat. While the qualitative high speed image data suggests that nucleate boiling is delayed or eliminated at higher F_c, it would be of value to determine the precise superheat at which nucleate boiling occurs for various F_c.

While the current experiments studied the effects of varying surface temperature, T_s, and F_c, the effects of initial droplet size, liquid density and viscosity, ambient air temperature, relative humidity, and SH feature type (i.e. ribs vs. posts) were not studied. It may be of value to determine what effect, if any, these parameters have on the heat transfer for various surfaces.

The experiments on sessile droplets could be extended to quiescent pools. Experiments with pool evaporation and boiling could yield different results than experiments with sessile droplets as droplet size is eliminated as a variable and local surface effects are reduced. In addition, using pools allows for more convenient and accurate normalization of heat transfer rates by liquid-solid contact area, allowing for calculation of heat transfer coefficients at temperatures above the saturation temperature.

REFERENCES

[1] Young, T., 1805. "An Essay on the Cohesion of Fluids." *Philosophical Transactions of the Royal Society of London,* **95**, January, pp. 65–87. 1

[2] Wenzel, R., 1936. "Resistance of solid surfaces to wetting by water." *Industrial and Engineering Chemistry,* **28**(8), August, pp. 988–994. 2

[3] Cassie, A., and Baxter, S., 1944. "Wettability of porous surfaces." *Transactions of the Faraday Society,* **40**(0), June, pp. 546–551. 3, 11

[4] Dupuis, A., and Yeomans, J. M., 2006. "Dynamics of sliding drops on superhydrophobic surfaces." *Europhysics Letters,* **75**(1), July, pp. 105–111. 3

[5] Quere, D., 2005. "Non-sticking drops." *Reports on Progress in Physics,* **68**(11), November, pp. 2495–2532. 3

[6] Kusumaatmaja, H., Leopoldes, L., Dupuis, A., and Yeomans, J. M., 2006. "Drop dynamics on chemically patterned surfaces." *Europhysics Letters,* **73**(5), March, pp. 740–746. 3

[7] Wang, Z., Lopez, C., Hirsa, A., and Koratkar, N., 2007. "Impact dynamics and rebound of water droplets on superhydrophobic carbon nanotube arrays." *Applied Physics Letters,* **91**(2), July, p. 023105. 3, 4

[8] Jung, Y., and Bhushan, B., 2007. "Wetting transition of water droplets on superhydrophobic patterned surface." *Scripta Materialia,* **57**(12), Decemeber, pp. 1057–1060. 3, 4

[9] Hyvaluoma, J., and Timonen, J., 2009. "Impact states and energy dissipation in bouncing and non-bouncing droplets." *Journal of Statistical Mechanics*, June, p. P06010. 3

[10] Ou, J., Perot, B., and Rothstein, J., 2004. "Laminar drag reduction in microchannels using ultrahydrophobic surfaces." *Physics of Fluids,* **16**(12), November, p. 4635. 4

[11] Ou, J., and Rothstein, J., 2005. "Direct velocity measurements of the flow past drag-reducing ultrahydrophobic surfaces." *Physics of Fluids,* **17**(10), October, p. 103606. 4

[12] Davies, J., Maynes, D., Webb, B. W., and Woolford, B., 2006. "Laminar flow in a microchannel with superhydrophobic walls exhibiting transverse ribs." *Physics of Fluids,* **18**(8), August, p. 087110. 4, 5

[13] Daniello, R., Waterhouse, N., and Rothstein, J., 2009. "Drag reduction in turbulent flows over superhydrophobic surfaces." *Physics of Fluids,* **21**(8), August, p. 085103. 4, 5

[14] Fukuda, K., Tokunaga, J., Nobunaga, T., Nakatani, T., Iwasaki, T., and Kunitake, Y., 2000. "Frictional drag reduction with air lubricant over a super-water-repellent surface." *Journal of Marine Science and Technology,* **5**(3), December, pp. 123–130. 4

[15] Joseph, P., Cottin-Bizonne, C., Benoit, J. M., Ybert, C., Journet, C., Tabeling, P., and Bocquet, L., 2006. "Sippage of Water Past Superhydrophobic Carbon Nanotube Forests in Microchannels." *Physical Review Letters,* **97**(15), October, p. 156104. 4

[16] Truesdell, R., Mammoli, A., Vorobieff, P., van Swol, F., and Brinker, C. J., 2006. "Drag Reduction on a Patterned Superhydrophobic Surface." *Physical Review Letters,* **97**(4), July, p. 044504. 4

[17] Fukagata, K., Kasagi, N., and Koumoutsakos, P., 2006. "A theoretical prediction of friction drag reduction in turbulent flow by superhydrophobic surfaces." *Physics of Fluids,* **18**(5), May, p. 051703. 4

[18] Martell, M., Perot, J., and Rothstein, J., 2009. "Direct numerical simulations of turbulent flows over superhydrophobic surfaces." *Journal of Fluid Mechanics,* **620**, February, pp. 31–41. 4

[19] Incropera, F., DeWitt, D., Bergman, T., and Lavine, A., 2007. *Fundamentals of Heat and Mass Transfer, 6th Ed.*. John Wiley & Sons, Hoboken, NJ. 5, 6

[20] Takata, Y., Hidaka, S., and Uraguchi, T., 2006. "Boiling Feature on a Super Water-Repellent Surface." *Heat Transfer Engineering,* **27**(8), September, pp. 25–30. 8, 37

[21] Phan, H., Caney, N., Marty, P., Colasson, S., and Gavillet, J., 2009. "Surface wettability control by nanocoating: The effects on pool boiling heat transfer and nucleation mechanism." *International Journal of Heat and Mass Transfer,* **52**(23–24), November, pp. 5459–5471. 8

[22] Betz, A., Jenkins, J., Kim, C., and Attinger, D., 2013. "Boiling heat transfer on superhydrophilic, superhydrophobic, and superbiphilic surfaces." *International Journal of Heat and Mass Transfer,* **57**(2), February, pp. 733–741. 8, 37

[23] Jo, H., Kang, S., Ahn, H., and Kim, M., 2010. "Experimental study of nucleate boiling performance on several types of the mixed-wettability pattern surface by micro/milli-sized hydrophobic patterns." In *Proceedings of the ASME 2010 8th International Conference on Nanochannels, Microchannels, and Minichannels*, ASME, AIP Publishing Paper number FEDSM-ICNMM2010-30428. 8, 37

[24] McHale, G., Aqil, S., Shirtcliffe, N., Newton, M., and Erbil, H., 2005. "Analysis of Droplet Evaporation on a Superhydrophobic Surface." *Langmuir,* **21**(24), October, pp. 11053–11060. 8, 9, 12, 37

[25] Zhang, X., Tan, S., Zhao, N., Guo, X., Zhang, X., Zhang, Y., and Xu, J., 2006. "Evaporation of Sessile Water Droplets on Superhydrophobic Natural Lotus and Biomimetic Polymer Surfaces." *ChemPhysChem,* **7**(10), October, pp. 2067–2070. 8, 9, 12, 37

[26] Sobac, B., and Brutin, D., 2011. "Triple-Line Behavior and Wettability Controlled by Nanocoated Substrates: Influence on Sessile Drop Evaporation." *Langmuir,* **27**(24), November, pp. 14999–15007. 8, 9, 13, 37

[27] Kulinich, S., and Farzaneh, M., 2009. "Effect of contact angle hysteresis on water droplet evaporation from super-hydrophobic surfaces." *Applied Surface Science,* **255**(7), January, pp. 4056–4060. 8, 13, 37

[28] Barthlott, W., and Neinhuis, C., 1997. "Purity of the sacred lotus, or escape from contamination in biological surfaces." *Planta,* **202**(1), April, pp. 1–8. 11

[29] Chen, W., Fadeev, A., Hsieh, M., Oner, D., Youngblood, J., and McCarthy, T., 1999. "Ultrahydrophobic and Ultralyophobic Surfaces: Some Comments and Examples." *Langmuir,* **15**(10), April, pp. 3395–3399. 11

[30] Blossey, R., 2003. "Self-cleaning surfaces–virtual realities." *Nature Materials,* **2**(5), May, pp. 301–306. 11

[31] Birdi, K., Vu, D., and Winter, A., 1989. "A study of the evaporation rates of small water drops placed on a solid surface." *The Journal of Physical Chemistry,* **93**(9), May, pp. 3702–3703. 12, 37

[32] Grandas, L., Santini, R., and Tadrist, L., 2004. "Heat Transfer Induced by Evaporation of a Sessile Drop: Influence of Wetting Surface." *AIP Conference Proceedings,* **699**, February, pp. 156–163. 12, 13, 37

[33] Chandra, S., di Marzo, M., Qiao, Y., and Tartarini, P., 1996. "Effect of liquid-solid contact angle on droplet evaporation." *Fire Safety Journal,* **27**(2), September, pp. 141–158. 13, 37

[34] Crafton, E., and Black, W., 2004. "Heat transfer and evaporation rates of small liquid droplets on heated horizontal surfaces." *International Journal of Heat and Mass Transfer,* **47**(6–7), March, pp. 1187–1200. 13, 37

[35] Fick, A., 1855. "Ueber diffusion." *Annalen der Physik,* **170**(1), pp. 59–86. 21

[36] Godsave, G., 1953. "Studies of the combustion of drops in a fuel spray–the burning of single drops of fuel." *Symposium (International) on Combustion,* **4**(1), pp. 818–830. 21

[37] Hays, R., Crockett, J., Maynes, D., and Webb, B. W., 2013. "Thermal transport to sessile droplets on superhydophobic surfaces with rib and cavity features." In *Proceedings of the ASME 2013 International Mechanical Engineering Congress & Exposition*, ASME, AIP Publishing Paper number IMECE2013-63780. 40, 43

APPENDIX A. HARDWARE SPECIFICATIONS

This appendix presents the detailed specifications for the hardware used in the experimental setup.

A.1 Infrared camera

Manufacturer: FLIR Systems

Model: ThermaCAM SC500

Instantaneous field of view: 1.3 mrad

Thermal sensitivity: 0.07 °C at 30 °C

Detector type: Uncooled Focal Plane Array (FPA), 320 x 240 pixels

Spectral range: 7.5–13 µm, built-in atmospheric filter with cut-on at 7.5 µm

Object temperature measurement range: 0–500 °C

Accuracy: ±2% of range or ± 2 °C

Atmospheric transmission correction: Automatic based on distance, atmospheric temperature and humidity

Temperature compensation: Background temperature emissivity correction and distance

A.2 CCD video cameras

Manufacturer: Arm Electronics

Model: C420

Signal system: NTSC

Image sensor: 1/3" color CCD

Resolution: 420 lines

Number of pixels: 768 x 494

Lens: Navitar Zoom 7000

Minimum illumination: 0.5 lux

Signal-to-noise ratio: $> 48\,\mathrm{dB}$

Sync: Internal

A.3 Hygrometer/thermometer

Manufacturer: Control Company

Model: 4087 Traceable

Humidity range: 10–95%

Relative humidity resolution: 0.01%

Relative humidity accuracy: $\pm 1.5\%$

Temperature range: 0–50 °C

Temperature resolution: 0.01 °F

Temperature accuracy: $\pm 0.4\,^{\circ}\mathrm{C}$ at tested points

Response time: 30–210 s

APPENDIX B. MATLAB CODE

The MATLAB code used to process the experimental data is presented in this appendix. The first set of code was used in post-processing the raw CCD video frames to extract geometric information such as droplet volume and contact angle. The next section's code was used for smoothing the droplet volume data so that cleaner derivatives could be computed. The code in the final section was used to analyze the temperature and geometry data and create the plots shown in this thesis.

B.1 Video post-processing code

```
%% Clear all variables and figures:
clear, close all

%% Perform calibration

% Read in calibration images:
imleft  = imread('..\CCD Data\Set 12\calleft.jpg');
imright = imread('..\CCD Data\Set 12\calright.jpg');

Lx = 0.003171; % width of calibration object
Ly = 0.003171; % height of calibration object

imscale = ccdcal(imleft,imright,Lx,Ly); % find calibration constants

%% Create list of data files to process:
testrun = [...
    '8RC1201';
    '8RC1202';
```

```
    '8RC1203';
    '8RC1401';
    '8RC1402';
    '8RC1403';
    '8RC1601';
    '8RC1602';
    '8RC1603';
    '8RC1801';
    '8RC1802';
    '8RC1803';
    '8RC2001';
    '8RC2002';
    '8RC2003';
    '8RC2201';
    '8RC2202';
    '8RC2203';
    '8RC2301';
    '8RC2302';
    '8RC2303';
    '9RC1201';
    '9RC1202';
    '9RC1203';
    '9RC1401';
    '9RC1402';
    '9RC1403';
    '9RC1601';
    '9RC1602';
    '9RC1603';
    ];

%% Loop through each pair of video files and process:
for k = 1:size(testrun,1)

    % Get the rotation and cropping data:
    cropdata = xlsread('..\Processed Data\rotcrop data.xlsx',...
        testrun(k,1:3));
```

```
55
56      % Find the row number for the current data set:
57      if str2double(testrun(k,4:6)) <= 110
58          cellnum = ((str2double(testrun(k,4:6))/10 - 5) - 1)*3 +...
59              str2double(testrun(k,7));
60      else
61          cellnum = (ceil(str2double(testrun(k,4:6))/20) - 1)*3 +...
62              str2double(testrun(k,7));
63      end
64
65      % Extract the rotation angles and crop locations:
66      lrotangl = cropdata(cellnum,1);
67      rrotangl = cropdata(cellnum,2);
68      lcrops   = cropdata(cellnum,3);
69      rcrops   = cropdata(cellnum,4);
70
71      %% Initialize the video frames:
72
73      % Read in droplet videos:
74      dropleft  = VideoReader(['..\CCD Data\Set 12\L' testrun(k,:) '.avi']);
75      dropright = VideoReader(['..\CCD Data\Set 12\R' testrun(k,:) '.avi']);
76
77      % Get the number of frames and duration of each video:
78      numFrames = [dropleft.NumberOfFrames dropright.NumberOfFrames];
79      duration  = min([dropleft.Duration dropright.Duration]);
80
81      % Figure out the true frame sampling interval by rejecting identical
82      % frames:
83      framesamp = 0;
84      i         = 1;
85      j         = 0;
86      while framesamp < 1
87          while j < 1
88              leftsamp1 = read(dropleft,i);
89              leftsamp2 = read(dropleft,i+1);
90              leftsamp  = leftsamp2 - leftsamp1;
```

```
91              framecond = any(any(leftsamp));
92              if framecond == 1;
93                  framesamp1  = i;
94                  j           = 1;
95              end
96              i = i + 1;
97          end
98          while j < 2
99              leftsamp1   = read(dropleft,i);
100             leftsamp2   = read(dropleft,i+1);
101             leftsamp    = leftsamp2 - leftsamp1;
102             framecond   = any(any(leftsamp));
103             if framecond == 1;
104                 framesamp2  = i;
105                 j           = 2;
106             end
107             i = i + 1;
108         end
109         framesamp = framesamp2 - framesamp1;
110     end
111
112     % Find the total number of frames to use:
113     imax = floor(min(numFrames)/framesamp);
114
115     % Initialize volume, contact area, and contact angle vectors:
116     V     = zeros(imax,1);
117     Ab    = zeros(imax,1);
118     theta = zeros(imax,1);
119
120     %% Loop through each pair of video frames and process:
121     for i = 1:imax
122
123         % Display a progress indicator in the command window:
124         clc
125         progress = ['Data point ' num2str(i) '/' num2str(imax) '; File '...
126             num2str(k) '/' num2str(size(testrun,1))]
```

```
127
128         %% Read in the current frames and convert to grayscale:
129
130         % Read in current video frames:
131         left  = read(dropleft,i*framesamp-framesamp+1);
132         right = read(dropright,i*framesamp-framesamp+1);
133
134         % Convert to grayscale:
135         left  = rgb2gray(left);
136         right = rgb2gray(right);
137
138 %         figure(1), imshow(left), figure(2), imshow(right)
139
140         %% Crop and resize images:
141
142         % Convert images from 8-bit to 0--1 scale:
143         left2  = double(left)/255;
144         right2 = double(right)/255;
145 %         left        = double(imcrop(left,[9 1 703 480]))/255;
146 %         right       = double(imcrop(right,[9 1 703 480]))/255;
147
148         % Setup original (640x480) and final (800x600) resolution vectors:
149         x  = linspace(0,1,640);
150         xi = linspace(0,1,800);
151         y  = linspace(0,1,480);
152         yi = linspace(0,1,600);
153
154         % Resize images from 640x480 to 800x600
155         left2  = interp2(x,y,left2,xi,yi');
156         right2 = interp2(x,y,right2,xi,yi');
157
158 %         figure(1), imshow(left2), figure(2), imshow(right2)
159
160         %% Pad images on sides and top with whitespace:
161         left3  = [ones(30,860); ones(600,30) left2 ones(600,30)];
162         right3 = [ones(30,860); ones(600,30) right2 ones(600,30)];
```

```
163
164 %         figure(1), imshow(left3), figure(2), imshow(right3)
165
166         %% Rotate and crop images:
167         [left4 right4] = rotcrop2(left3,right3,[lrotangl rrotangl],...
168             lcrops,rcrops);
169
170 %         figure(1), imshow(left4), figure(2), imshow(right4)
171
172         %% Convert images to binary:
173
174         % Find light intensity threshold levels:
175         llevel = 0.7*mean(mean(left4));
176         rlevel = 0.7*mean(mean(right4));
177
178         % Convert images from grayscale to binary:
179         left5  = imcomplement(im2bw(left4,llevel));
180         right5 = imcomplement(im2bw(right4,rlevel));
181
182 %         figure(1), imshow(left5), figure(2), imshow(right5)
183
184         %% Fill in droplet shape:
185
186         % Create hulls of all objects in binary images:
187         left6  = bwconvhull(left5,'objects');
188         right6 = bwconvhull(right5,'objects');
189
190         % Find the area (in pixels) of each object in the binary images:
191         areasleft  = regionprops(left6,'Area');
192         areasright = regionprops(right6,'Area');
193
194         % Remove all but the largest objects:
195         if max([areasleft.Area]) ~= 0
196             left6  = bwareaopen(left6,max([areasleft.Area]) - 1);
197         end
198         if max([areasright.Area]) ~= 0
```

```
199             right6 = bwareaopen(right6,max([areasright.Area]) - 1);
200         end
201
202         % Create hulls of droplet objects:
203         left6  = bwconvhull(left6);
204         right6 = bwconvhull(right6);
205
206 %         figure(1), imshow(left6), figure(2), imshow(right6)
207
208         %% Find contact area:
209
210         % Find the contact diameter for each image:
211         contdialeft  = imscale(1,1)*...
212             size(left6(left6(size(left6,1),:) == 1),2);
213         contdiaright = imscale(2,1)*...
214             size(right6(right6(size(right6,1),:) == 1),2);
215
216         % Find the contact area according to each image:
217         contarealeft  = 0.25*pi*contdialeft^2;
218         contarearight = 0.25*pi*contdiaright^2;
219
220         % Average the contact areas from each image:
221         Ab(i) = 0.5*(contarealeft + contarearight);
222
223         %% Find volume:
224
225         % Initialize a vector of thin droplet volume disks:
226         diskradleft  = zeros(size(left6,1),1);
227         diskradright = zeros(size(right6,1),1);
228
229         % Find the cross-sectional area of each volume disk:
230         for j = 2:size(left6,1)
231             diskradleft(j)  = 0.5*imscale(1,1)*...
232                 size(left6(left6(j,:) == 1),2);
233         end
234         for j = 2:size(right6,1)
```

```
235             diskradright(j) = 0.5*imscale(2,1)*...
236                 size(right6(right6(j,:) == 1),2);
237         end
238 
239         % Find the droplet volume according to each image by summing disks:
240         dropvolleft  = sum(imscale(1,2)*pi*diskradleft.^2);
241         dropvolright = sum(imscale(2,2)*pi*diskradright.^2);
242 
243         % Average the volumes from each image:
244         V(i) = 0.5*(dropvolleft + dropvolright);
245 
246         %% Find contact angle:
247 
248         % Find perimeter of droplet shape:
249         left7  = bwperim(left6);
250         right7 = bwperim(right6);
251 
252         % Convert perimeter to x-y coordinate points:
253         left7           = left7(floor(2*size(left7,1)/3):end-1,:);
254         right7          = right7(floor(2*size(right7,1)/3):end-1,:);
255         [yleft xleft]   = find(left7 == 1);
256         [yright xright] = find(right7 == 1);
257 
258         % Fit ellipse to perimeter points (if they exist):
259         if isempty(yleft)
260             continue
261         elseif isempty(yright)
262             continue
263         else
264             if (max(yleft) - min(yleft)) < 2
265                 continue
266             elseif (max(yright) - min(yright)) < 2
267                 continue
268             else
269                 lelps = fit_ellipse(xleft,yleft);
270                 relps = fit_ellipse(xright,yright);
```

```
271             end
272         end
273
274         % Find contact angles (if possible):
275         try
276
277             % Define first element and last element of vector:
278             firstelement = @(v) v(1);
279             lastelement  = @(v) v(end);
280
281             % Create multiplier to scale the ellipse dimensions properly:
282             leftmult  = imscale(1,2)/imscale(1,1);
283             rightmult = imscale(2,2)/imscale(2,1);
284
285             % Find the x-y coordinates of the left- and right-most droplet-
286             % substrate contact points:
287             YP1left  = firstelement(max(yleft(xleft <= lelps.X0_in)));
288             YP2left  = firstelement(max(yleft(xleft >= lelps.X0_in)));
289             XP1left  = firstelement(xleft(yleft == max(yleft)));
290             XP2left  = lastelement(xleft(yleft == max(yleft)));
291             YP1right = firstelement(max(yright(xright <= relps.X0_in)));
292             YP2right = firstelement(max(yright(xright >= relps.X0_in)));
293             XP1right = firstelement(xright(yright == max(yright)));
294             XP2right = lastelement(xright(yright == max(yright)));
295
296             % Transform the contact points to the ellipse coordinate frame:
297             XPP1left  = lelps.a*cos(atan2((YP1left - lelps.Y0_in)*...
298                 leftmult,XP1left - lelps.X0_in) - lelps.phi);
299             XPP2left  = lelps.a*cos(atan2((YP2left - lelps.Y0_in)*...
300                 leftmult,XP2left - lelps.X0_in) - lelps.phi);
301             XPP1right = relps.a*cos(atan2((YP1right - relps.Y0_in)*...
302                 rightmult,XP1right - relps.X0_in) - relps.phi);
303             XPP2right = relps.a*cos(atan2((YP2right - relps.Y0_in)*...
304                 rightmult,XP2right - relps.X0_in) - relps.phi);
305
306             % Find the contact angle at each side of the droplet:
```

```
307             thet1left  = atan2(-lelps.b*XPP1left,lelps.a^2*...
308                 sqrt(1 - XPP1left^2/lelps.a^2));
309             thet2left  = atan2(-lelps.b*XPP2left,lelps.a^2*...
310                 sqrt(1 - XPP2left^2/lelps.a^2));
311             thet1right = atan2(-relps.b*XPP1right,relps.a^2*...
312                 sqrt(1 - XPP1right^2/relps.a^2));
313             thet2right = atan2(-relps.b*XPP2right,relps.a^2*...
314                 sqrt(1 - XPP2right^2/relps.a^2));
315
316             % Put contact angles in quadrant I or II:
317             if YP1left >= lelps.Y0_in
318                 thet1left = pi - thet1left;
319             end
320             if YP2left >= lelps.Y0_in
321                 thet2left = pi + thet2left;
322             else
323                 thet2left = -thet2left;
324             end
325             if YP1right >= relps.Y0_in
326                 thet1right = pi - thet1right;
327             end
328             if YP2right >= relps.Y0_in
329                 thet2right = pi + thet2right;
330             else
331                 thet2right = -thet2right;
332             end
333
334             % Average contact angles from each droplet side and each image:
335             theta(i) = mean([thet1right thet2right thet1left thet2left]);
336
337         catch
338
339             continue
340
341         end
342
```

```
343     end
344
345     %% Output data:
346
347     % Create time vector:
348     t  = (linspace(0,duration,imax))';
349
350 %     Va     = V;
351 %     Aba    = Ab;
352 %     thetaa = theta;
353 %     ta     = t;
354 %     Vb     = V;
355 %     Abb    = Ab;
356 %     thetab = theta;
357 %     tb     = t;
358
359     % Output plots and spreadsheet file:
360 %     V = [Va; Vb]; Ab = [Aba; Abb]; theta = [thetaa; thetab]; t = [ta; tb+ta(end)];
361     figure(k)
362
363     subplot(1,3,1)
364     plot(t,V*10^9)
365     xlabel('Time (s)')
366     ylabel('Volume (\muL)')
367     title(testrun(k,:))
368
369     subplot(1,3,2)
370     plot(t,Ab*10^6)
371     xlabel('Time (s)')
372     ylabel('Contact area (mm^2)')
373
374     subplot(1,3,3)
375     plot(t,theta*180/pi)
376     xlabel('Times (s)')
377     ylabel('Contact angle (deg)')
378
```

```
    % Write data to Excel file
    xlswrite(['..\Processed Data\G' testrun(k,:) '.xlsx'],...
        {'t' 'V' 'A_b' 'theta'},'Sheet1','A1');
    xlswrite(['..\Processed Data\G' testrun(k,:) '.xlsx'],...
        [t V Ab theta],'Sheet1','A2');

end
```

B.2 Droplet volume smoothing code

```
% Smooths data sets

clear, close all

% Get dataset names:
datasets = [...
    '0SC1001';
    '0SC1002';
    '0SC1003';
    '0SC1101';
    '0SC1102';
    '0SC1103';
    '0SC1201';
    '0SC1202';
    '0SC1203';
    '0SC1301';
    '0SC1302';
    '0SC1303';
    '0SC1401';
    '0SC1402';
    '0SC1403';
    '0SC1501';
    '0SC1502';
    '0SC1503';
    '0SC1601';
```

```
26      '0SC1602';
27      '0SC1603';
28      '0SC1701';
29      '0SC1702';
30      '0SC1703';
31      '0SC1801';
32      '0SC1802';
33      '0SC1803';
34      '0SC1901';
35      '0SC1902';
36      '0SC1903';
37      '0SC2001';
38      '0SC2002';
39      '0SC2003';
40      '0SC2101';
41      '0SC2102';
42      '0SC2103';
43      '0SC2201';
44      '0SC2202';
45      '0SC2203';
46      '0SC2301';
47      '0SC2302';
48      '0SC2303';
49      '5RC1001';
50      '5RC1002';
51      '5RC1003';
52      '5RC1101';
53      '5RC1102';
54      '5RC1103';
55      '5RC1201';
56      '5RC1202';
57      '5RC1203';
58      '5RC1301';
59      '5RC1302';
60      '5RC1303';
61      '5RC1401';
```

```
62      '5RC1402';
63      '5RC1403';
64      '5RC1501';
65      '5RC1502';
66      '5RC1503';
67      '5RC1601';
68      '5RC1602';
69      '5RC1603';
70      '5RC1701';
71      '5RC1702';
72      '5RC1703';
73      '5RC1801';
74      '5RC1802';
75      '5RC1803';
76      '5RC1901';
77      '5RC1902';
78      '5RC1903';
79      '5RC2001';
80      '5RC2002';
81      '5RC2003';
82      '5RC2101';
83      '5RC2102';
84      '5RC2103';
85      '5RC2201';
86      '5RC2202';
87      '5RC2203';
88      '5RC2301';
89      '5RC2302';
90      '5RC2303';
91      '8RC1001';
92      '8RC1002';
93      '8RC1003';
94      '8RC1101';
95      '8RC1102';
96      '8RC1103';
97      '8RC1201';
```

```
98      '8RC1202';
99      '8RC1203';
100     '8RC1301';
101     '8RC1302';
102     '8RC1303';
103     '8RC1401';
104     '8RC1402';
105     '8RC1403';
106     '8RC1501';
107     '8RC1502';
108     '8RC1503';
109     '8RC1601';
110     '8RC1602';
111     '8RC1603';
112     '8RC1701';
113     '8RC1702';
114     '8RC1703';
115     '8RC1801';
116     '8RC1802';
117     '8RC1803';
118     '8RC1901';
119     '8RC1902';
120     '8RC1903';
121     '8RC2001';
122     '8RC2002';
123     '8RC2003';
124     '8RC2101';
125     '8RC2102';
126     '8RC2103';
127     '8RC2201';
128     '8RC2202';
129     '8RC2203';
130     '8RC2301';
131     '8RC2302';
132     '8RC2303';
133     '9RC1001';
```

```
134      '9RC1002';
135      '9RC1003';
136      '9RC1101';
137      '9RC1102';
138      '9RC1103';
139      '9RC1201';
140      '9RC1202';
141      '9RC1203';
142      '9RC1301';
143      '9RC1302';
144      '9RC1303';
145      '9RC1401';
146      '9RC1402';
147      '9RC1403';
148      '9RC1501';
149      '9RC1502';
150      '9RC1503';
151      '9RC1601';
152      '9RC1602';
153      '9RC1603';
154      '9RC1701';
155      '9RC1702';
156      '9RC1703';
157      '9RC1901';
158      '9RC1902';
159      '9RC1903';
160      ];
161
162  %% Set default smoothing parameters:
163  spanV  = 0.9;
164
165  for i = 1:size(datasets,1)
166
167  %     close all
168  %     breaklp = 0;
169
```

```
170     % Import data from dataset i:
171     data = xlsread(['..\Processed Data\G' datasets(i,:) '.xlsx']);
172     t    = data(:,1);
173     V    = data(:,2);
174
175 %     % Plot original data:
176 %     figure(1), subplot(211)
177 %     plot(t,V), title(datasets(i,:))
178 %     xlimV  = xlim;
179 %     ylimV  = ylim;
180 %
181 %     while breaklp < 1
182
183         % Smooth the data:
184         Vs  = smooth(V,spanV,'rloess');
185         ts  = t;
186
187 %         % Remove zero values:
188 %         Vssmall  = find(Vs-Vs(1)/10000<0);
189 %         Abssmall = find(Abs-Abs(1)/10000<0);
190 %         dataend  = min([Vssmall; Abssmall])-1;
191 %         ts       = t(1:dataend);
192 %         Vs       = Vs(1:dataend);
193 %         Abs      = Abs(1:dataend);
194 %
195 %         % Plot smoothed data:
196 %         figure(1), subplot(212)
197 %         plot(ts,Vs), axis([xlimV ylimV])
198 %
199 %         % Wait for user input:
200 %         prompt    = {'Span for V:'};
201 %         dlg_title = 'Change or keep current parameters?';
202 %         num_lines = 1;
203 %         def       = {num2str(spanV)};
204 %         options.Resize = 'on';
205 %         options.WindowStyle = 'normal';
```

```
%          answer    = inputdlg(prompt,dlg_title,num_lines,def,options);
%
%          % Check if parameters have changed:
%          if str2double(answer(1))==spanV
%              breaklp = 1;
%          else
%              spanV  = str2double(answer(1));
%          end
%
%      end

    %% Save the smoothed data:
    xlswrite(['..\Smoothed Data\S' datasets(i,:) '.xlsx'],[ts Vs])

end
```

B.3 Data analysis and plotting code

```
clear, close all

% Setup constants:
surftyp = ['0SC'; '5RC'; '8RC'; '9RC'];
surftemp = ['060'; '070'; '080'; '090'; '100'];
g = 9.81;
thermprops = [...
    273.15 1     2502 4217 1750 569 -68.05;...
    275    1     2497 4211 1652 574 -32.74;...
    280    1     2485 4198 1422 582 46.04;...
    285    1     2473 4189 1225 590 114.1;...
    290    1.001 2461 4184 1080 598 174;...
    295    1.002 2449 4181 959  606 227.5;...
    300    1.003 2438 4179 855  613 276.1;...
    305    1.005 2426 4178 769  620 320.6;...
    310    1.007 2414 4178 695  628 361.9;...
    315    1.009 2402 4179 631  634 400.4;...
```

```
    320    1.011 2390 4180 577  640 436.7;...
    325    1.013 2378 4182 528  645 471.2;...
    330    1.016 2366 4184 489  650 504;...
    335    1.018 2354 4186 453  656 535.5;...
    340    1.021 2342 4188 420  660 566;...
    345    1.024 2329 4191 389  668 595.4;...
    350    1.027 2317 4195 365  668 624.2;...
    355    1.03  2304 4199 343  671 652.3;...
    360    1.034 2291 4203 324  674 697.9;...
    365    1.038 2278 4209 306  677 707.1;...
    370    1.041 2265 4214 289  679 728.7;...
    373.15 1.044 2257 4217 279  680 750.1;...
    ];
rho      = thermprops(:,[1 2]);
rho(:,2) = 10^3./rho(:,2);
hfg      = thermprops(:,[1 3]);
hfg(:,2) = hfg(:,2)*1000;
mu       = thermprops(:,[1 5]);
mu(:,2)  = mu(:,2)/10^6;
nu       = mu;
nu(:,2)  = nu(:,2)./rho(:,2);
kf       = thermprops(:,[1 6]);
kf(:,2)  = kf(:,2)/1000;
bet      = thermprops(:,[1 7]);
bet(:,2) = bet(:,2)/10^6;
% figure(10), hold on
% plot(-3:1:-1,-3:1:-1,'r-','LineWidth',2)
% plot(-3:1:-1,-3:1:-1,'g-','LineWidth',2)
% plot(-3:1:-1,-3:1:-1,'b-','LineWidth',2)
% plot(-3:1:-1,-3:1:-1,'m-','LineWidth',2)
% figure(11), hold on
% plot(-3:1:-1,-3:1:-1,'r-','LineWidth',2)
% plot(-3:1:-1,-3:1:-1,'g-','LineWidth',2)
% plot(-3:1:-1,-3:1:-1,'b-','LineWidth',2)
% plot(-3:1:-1,-3:1:-1,'m-','LineWidth',2)
% figure(12), hold on
```

```
% plot(-3:1:-1,-3:1:-1,'r-','LineWidth',2)
% plot(-3:1:-1,-3:1:-1,'g-','LineWidth',2)
% plot(-3:1:-1,-3:1:-1,'b-','LineWidth',2)
% plot(-3:1:-1,-3:1:-1,'m-','LineWidth',2)
% figure(13), hold on
% plot(-3:1:-1,-3:1:-1,'r-','LineWidth',2)
% plot(-3:1:-1,-3:1:-1,'g-','LineWidth',2)
% plot(-3:1:-1,-3:1:-1,'b-','LineWidth',2)
% plot(-3:1:-1,-3:1:-1,'m-','LineWidth',2)

Gr = [];
Nu = [];

%% Get relevant data:
for i = 4

    switch i
        case 1
            lincol = 'r';
            marktyp = '+';
        case 2
            lincol = 'g';
            marktyp = 'o';
        case 3
            lincol = 'b';
            marktyp = 's';
        case 4
            lincol = 'm';
            marktyp = '^';
        case 5
            lincol = 'c';
            marktyp = 'd';
    end

    for j = 1:size(surftemp,1)

```

```
90          if j==5 && i==4
91              t_e(j) = 0;
92              T_s(j) = 0;
93              continue
94          end
95
96          for k = 1:3
97
98              geomdata = xlsread(['..\Processed Data\G' surftyp(i,:) surftemp(j,:) num2str(k)
99              smoothdata = xlsread(['..\Smoothed Data\S' surftyp(i,:) surftemp(j,:) num2str(k
100             tempdata = xlsread(['..\Processed Data\I' surftyp(i,:) surftemp(j,:) num2str(k)
101             conddata = xlsread(['..\Processed Data\Cond' surftyp(i,:) num2str(k) '.xls']);
102
103             Ts = conddata(j,2)+273.15;
104             Tinf = (conddata(j,3) + 459.67)*5/9;
105             RH = conddata(j,4);
106
107             V = smoothdata(:,2);
108             D3 = find(abs(V-pi*0.003^3/6)==min(abs(V-pi*0.003^3/6)));
109             t = geomdata(D3:end,1)-geomdata(D3,1);
110             V = smoothdata(D3:end,2);
111             Ab = geomdata(D3:end,3);
112
113             Td = tempdata(:,2);
114             ttemp = tempdata(:,1);
115             tD3 = find(abs(ttemp-geomdata(D3,1))==min(abs(ttemp-geomdata(D3,1))));
116             Td = Td(tD3:end);
117             ttemp = ttemp(tD3:end)-tempdata(tD3,1);
118
119 %             switch k
120 %                 case 1
121 %                     V1 = V;
122 %                     Ab1 = Ab;
123 %                     t1 = t;
124 %                     Td1 = Td;
125 %                     ttemp1 = ttemp;
```

```
126 %                     Ts1 = Ts;
127 %                     Tinf1 = Tinf;
128 %                     RH1 = RH;
129 %                 case 2
130 %                     V2 = V;
131 %                     Ab2 = Ab;
132 %                     t2 = t;
133 %                     Td2 = Td;
134 %                     ttemp2 = ttemp;
135 %                     Ts2 = Ts;
136 %                     Tinf2 = Tinf;
137 %                     RH2 = RH;
138 %                 case 3
139 %                     V3 = V;
140 %                     Ab3 = Ab;
141 %                     t3 = t;
142 %                     Td3 = Td;
143 %                     ttemp3 = ttemp;
144 %                     Ts3 = Ts;
145 %                     Tinf3 = Tinf;
146 %                     RH3 = RH;
147 %             end
148 %
149 %         end
150 %
151 %         geom_length = max([length(t1) length(t2) length(t3)]);
152 %         temp_length = max([length(ttemp1) length(ttemp2) length(ttemp3)]);
153 %
154 %         V1 = [V1; zeros(geom_length-length(V1),1)];
155 %         V2 = [V2; zeros(geom_length-length(V2),1)];
156 %         V3 = [V3; zeros(geom_length-length(V3),1)];
157 %         Ab1 = [Ab1; zeros(geom_length-length(Ab1),1)];
158 %         Ab2 = [Ab2; zeros(geom_length-length(Ab2),1)];
159 %         Ab3 = [Ab3; zeros(geom_length-length(Ab3),1)];
160 %         Td1 = [Td1; zeros(temp_length-length(Td1),1)];
161 %         Td2 = [Td2; zeros(temp_length-length(Td2),1)];
```

```
162 %         Td3 = [Td3; zeros(temp_length-length(Td3),1)];
163 %
164 %         Ts_avg = mean([Ts1 Ts2 Ts3]);
165 %         Tinf_avg = mean([Tinf1 Tinf2 Tinf3]);
166 %         RH_avg = mean([RH1 RH2 RH3]);
167 %         V_avg = mean([V1 V2 V3],2);
168 %         Ab_avg = mean([Ab1 Ab2 Ab3],2);
169 %         t_col = find([length(t1) length(t2) length(t3)]==max([length(t1) length(t2) lengt
170 %         switch t_col
171 %             case 1
172 %                 t_avg = t1;
173 %             case 2
174 %                 t_avg = t2;
175 %             case 3
176 %                 t_avg = t3;
177 %         end
178 %
179 %
180 %         Td_avg = mean([Td1 Td2 Td3],2);
181 %         ttemp_col = find([length(ttemp1) length(ttemp2) length(ttemp3)]==max([length(tte
182 %         switch ttemp_col
183 %             case 1
184 %                 ttemp_avg = ttemp1;
185 %             case 2
186 %                 ttemp_avg = ttemp2;
187 %             case 3
188 %                 ttemp_avg = ttemp3;
189 %         end
190 %
191 %         V_avg_i = interp1(t_avg,V_avg,ttemp_avg);
192 %
193 %         figure(3)
194 %         plot(t_avg,V_avg*10^9,lincol)
195 %         hold on
196 %         figure(4)
197 %         plot(t_avg,Ab_avg*10^6,lincol)
```

```
198 %           hold on
199 %           figure(5)
200 %           plot(ttemp_avg,Td_avg-273.15,lincol)
201 %           hold on
202
203           V_curve  = polyfit(t_avg(1:t_end),V_avg(1:t_end),2);
204           dVdt     = polyval(polyder(V_curve),t_avg(1:t_end));
205           Ab_curve = polyfit(t_avg(1:t_end),Ab_avg(1:t_end),2);
206           Ab_fit   = polyval(Ab_curve,t_avg(1:t_end));
207
208           Td_i = interp1(ttemp_avg,Td_avg,t_avg);
209           Td_curve = polyfit(t_avg(1:t_end),Td_i(1:t_end),1);
210           Td_fit = polyval(Td_curve,t_avg(1:t_end));
211
212           powr = -dVdt.*interp1(rho(:,1),rho(:,2),Td_fit).*interp1(hfg(:,1),hfg(:,2),Td_fit),
213           flux = powr./Ab_fit;
214
215           Gr1 = g*interp1(bet(:,1),bet(:,2),Td_fit).*(Ts_avg - Td_fit).*V_avg(1:t_end)./(inte
216           Gr2 = g*interp1(bet(:,1),bet(:,2),Td_fit).*(Ts_avg - Td_fit).*Ab_fit.^1.5./(interp1
217           Nu1 = flux.*V_avg(1:t_end).^(1/3)./(Ts_avg - Td_fit)./interp1(kf(:,1),kf(:,2),Td_fi
218           Nu2 = flux.*Ab_fit.^0.5./(Ts_avg - Td_fit)./interp1(kf(:,1),kf(:,2),Td_fit);
219 %           if j < 4
220           Gr = [Gr; Gr1];
221           Nu = [Nu; Nu2];
222 %           end
223
224
225 %           figure(10)
226 %           semilogx(Gr1,Nu2,lincol,'LineWidth',2)
227 %           text(Gr1(1),Nu2(1),['T_s = ' num2str(str2double(surftemp(j,:))) ' \circC'])
228 %           hold on
229 %           figure(11)
230 %           semilogy(Gr1,Nu2,lincol,'LineWidth',2)
231 %           text(Gr1(1),Nu2(1),['T_s = ' num2str(str2double(surftemp(j,:))) ' \circC'])
232 %           hold on
233           figure(12)
```

```
234         semilogx(Gr1,Nu2,lincol,'LineWidth',2)
235         text(Gr1(1),Nu2(1),['T_s = ' num2str(str2double(surftemp(j,:))) ' \circC'])
236         hold on
237
238 %         h = flux./(Ts_avg - Td_fit);
239 %         figure(9)
240 %         hold on
241 %         plot(V_avg(1:t_end)*10^9,h,lincol);
242 %
243 %         dtbl = floor(t_end/20);
244 %         V_tbl = V_avg(1:dtbl:t_end);
245 %         Ac_tbl = Ab_fit(1:dtbl:t_end);
246 %         Td_tbl = Td_fit(1:dtbl:t_end);
247 %         Ts_tbl = repmat(Ts_avg,length(V_tbl),1);
248 %         Tinf_tbl = repmat(Tinf_avg,length(V_tbl),1);
249 %         RH_tbl = repmat(RH_avg/100,length(V_tbl),1);
250 %         q_tbl = powr(1:dtbl:t_end);
251 %         flux_tbl = flux(1:dtbl:t_end);
252 %
253 %         xlswrite('..\Processed Data\data summary.xlsx',[V_tbl Ac_tbl Td_tbl Ts_tbl Tinf_t
254 %
255 %         figure(8)
256 %         hold on
257 %         plot(V_avg(1:t_end),Td_fit-273.15,V_avg(1:t_end),Td_i(1:t_end)-273.15,lincol)
258 %         ylim([0 str2double(surftemp(j,:))])
259 %         figure(1)
260 %         hold on
261 %         plot(V_avg(1:t_end)*10^9,powr,lincol)
262 %         figure(2)
263 %         hold on
264 %         plot(V_avg(1:t_end)*10^9,flux*10^-6,lincol)
265 %         figure(7)
266 %         hold on
267 %         plot(V_avg_i*10^9,Td_avg-273.15,lincol)
268
269 %         t_e(j) = mean([t1(end) t2(end) t3(end)]);
```

```
%          T_s(j) = mean(Ts);

    end

%     figure(6)
%     hold on
%     plot(T_s,t_e,[lincol marktyp])

end

%% Add exponential fit line:
[GrNufit,gof] = fit(Gr,Nu,'power1');
x = 10.^(0:0.1:5);
y = feval(GrNufit,x);
figure(12)
semilogx(x,y,'k:','LineWidth',2)
% text(mean(Gr),mean(Nu),['Nu = ' num2str(1/GrNufit.b) 'ln(Gr) - ' num2str(log(GrNufit.a))
text(mean(Gr),mean(Nu),['Nu = ' num2str(GrNufit.a) 'Gr^{' num2str(GrNufit.b) '}, R^2 = ' nu

%% Edit plots:
% figure(1)
% set(gca,'FontSize',15,'FontName','Times')
% set(gca,'XMinorTick','on','YMinorTick','on')
% xlabel('$V\,(mm^3)$','Interpreter','latex')
% ylabel('$q\,(W)$','Interpreter','latex')
% title(['Volume dependence of heat input at T_s = ' num2str(str2double(surftemp(j,:))) ' \
% % ap = get(gca,'pos');
% set(gcf,'PaperPosition',[1 1 7 5.5])
% set(gcf,'units',get(gcf,'PaperUnits'),'Position',get(gcf,'PaperPosition'))
% legend('F_c = 0 (HPo)','F_c = 0.5','F_c = 0.8','F_c = 0.95','Location','SouthEast')
% set(gcf,'Color','w')
%
% figure(2)
% set(gca,'FontSize',15,'FontName','Times')
% set(gca,'XMinorTick','on','YMinorTick','on')
% xlabel('$V\,(mm^3)$','Interpreter','latex')
```

```
% ylabel('$q^{\prime\prime}_{avg}\,(W/mm^2)$','Interpreter','latex')
% title(['Volume dependence of average interfacial heat flux at T_s = ' num2str(str2double
% % ap = get(gca,'pos');
% set(gcf,'PaperPosition',[1 1 7 5.5])
% set(gcf,'units',get(gcf,'PaperUnits'),'Position',get(gcf,'PaperPosition'))
% legend('F_c = 0 (HPo)','F_c = 0.5','F_c = 0.8','F_c = 0.95','Location','NorthEast')
% set(gcf,'Color','w')

% figure(3)
% set(gca,'FontSize',15,'FontName','Times')
% set(gca,'XMinorTick','on','YMinorTick','on')
% xlabel('$t\,(s)$','Interpreter','latex')
% ylabel('$V\,(mm^3)$','Interpreter','latex')
% title(['Transient droplet volume at T_s = ' num2str(str2double(surftemp)) ' \circC'])
% % ap = get(gca,'pos');
% set(gcf,'PaperPosition',[1 1 7 5.5])
% set(gcf,'units',get(gcf,'PaperUnits'),'Position',get(gcf,'PaperPosition'))
% legend('F_c = 0 (HPi)','F_c = 0 (HPo)','F_c = 0.5','F_c = 0.8','Location','NorthEast')
% set(gcf,'Color','w')
%
% figure(4)
% set(gca,'FontSize',15,'FontName','Times')
% set(gca,'XMinorTick','on','YMinorTick','on')
% xlabel('$t\,(s)$','Interpreter','latex')
% ylabel('$A_c\,(mm^2)$','Interpreter','latex')
% title(['Transient droplet contact area at T_s = ' num2str(str2double(surftemp)) ' \circC
% % ap = get(gca,'pos');
% set(gcf,'PaperPosition',[1 1 7 5.5])
% set(gcf,'units',get(gcf,'PaperUnits'),'Position',get(gcf,'PaperPosition'))
% legend('F_c = 0 (HPi)','F_c = 0 (HPo)','F_c = 0.5','F_c = 0.8','Location','NorthEast')
% set(gcf,'Color','w')
%
% figure(5), ylim([25 str2double(surftemp)])
% set(gca,'FontSize',15,'FontName','Times')
% set(gca,'XMinorTick','on','YMinorTick','on')
% xlabel('$t\,(s)$','Interpreter','latex')
```

```
% ylabel('$T_d\,(^{\circ}C)$','Interpreter','latex')
% title(['Transient droplet temperature at T_s = ' num2str(str2double(surftemp)) ' \circC'
% % ap = get(gca,'pos');
% set(gcf,'PaperPosition',[1 1 7 5.5])
% set(gcf,'units',get(gcf,'PaperUnits'),'Position',get(gcf,'PaperPosition'))
% legend('F_c = 0 (HPi)','F_c = 0 (HPo)','F_c = 0.5','F_c = 0.8','Location','SouthWest')
% set(gcf,'Color','w')
%
% figure(6), ylim([50 450]), xlim([55 105])
% set(gca,'FontSize',15,'FontName','Times')
% set(gca,'XMinorTick','on','YMinorTick','on')
% xlabel('$T_s\,(^{\circ}C)$','Interpreter','latex')
% ylabel('$t_e\,(s)$','Interpreter','latex')
% title('Droplet evaporation time')
% % ap = get(gca,'pos');
% set(gcf,'PaperPosition',[1 1 7 5.5])
% set(gcf,'units',get(gcf,'PaperUnits'),'Position',get(gcf,'PaperPosition'))
% legend('F_c = 0 (HPo)','F_c = 0.5','F_c = 0.8','F_c = 0.95','Location','NorthEast')
% set(gcf,'Color','w')

% figure(7), ylim([30 str2double(surftemp)])
% set(gca,'FontSize',15,'FontName','Times')
% set(gca,'XMinorTick','on','YMinorTick','on')
% xlabel('$V\,(mm^3)$','Interpreter','latex')
% ylabel('$T_d\,(^{\circ}C)$','Interpreter','latex')
% title(['Droplet temperature vs. droplet volume at T_s = ' num2str(str2double(surftemp))
% % ap = get(gca,'pos');
% set(gcf,'PaperPosition',[1 1 7 5.5])
% set(gcf,'units',get(gcf,'PaperUnits'),'Position',get(gcf,'PaperPosition'))
% legend('F_c = 0 (HPo)','F_c = 0.5','F_c = 0.8','F_c = 0.95','Location','SouthEast')
% set(gcf,'Color','w')

% figure(9)
% set(gca,'FontSize',15,'FontName','Times')
% set(gca,'XMinorTick','on','YMinorTick','on')
% xlabel('$V\,(mm^3)$','Interpreter','latex')
```

```
% ylabel('$h\,(W/m^2\{bullet}K)$','Interpreter','latex')
% title(['Heat transfer coefficient vs. droplet volume at T_s = ' num2str(str2double(surfte
% % ap = get(gca,'pos');
% set(gcf,'PaperPosition',[1 1 7 5.5])
% set(gcf,'units',get(gcf,'PaperUnits'),'Position',get(gcf,'PaperPosition'))
% legend('F_c = 0 (HPo)','F_c = 0.5','F_c = 0.8','F_c = 0.95','Location','NorthEast')
% set(gcf,'Color','w')

% figure(10)
% set(gca,'FontSize',15,'FontName','Times')
% set(gca,'XMinorTick','on','YMinorTick','on')
% xlabel('$Gr = \frac{g\beta(T_s - T_d)V}{\nu^2}$','Interpreter','latex')
% ylabel('$Nu = \frac{q"V^{1/3}}{(T_s - T_d)k}$','Interpreter','latex')
% title('Nu vs. Gr for F_c = 0.8')
% % ap = get(gca,'pos');
% set(gcf,'PaperPosition',[1 1 7 5.5])
% set(gcf,'units',get(gcf,'PaperUnits'),'Position',get(gcf,'PaperPosition'))
% % legend('F_c = 0 (HPo)','F_c = 0.5','F_c = 0.8','F_c = 0.95','Location','SouthEast')
% set(gcf,'Color','w')
%
% figure(11)
% set(gca,'FontSize',15,'FontName','Times')
% set(gca,'XMinorTick','on','YMinorTick','on')
% xlabel('$Gr = \frac{g\beta(T_s - T_d)A_c^{3/2}}{\nu^2}$','Interpreter','latex')
% ylabel('$Nu = \frac{q"A_c^{1/2}}{(T_s - T_d)k}$','Interpreter','latex')
% title('Nu vs. Gr for F_c = 0.8')
% % ap = get(gca,'pos');
% set(gcf,'PaperPosition',[1 1 7 5.5])
% set(gcf,'units',get(gcf,'PaperUnits'),'Position',get(gcf,'PaperPosition'))
% % legend('F_c = 0 (HPo)','F_c = 0.5','F_c = 0.8','F_c = 0.95','Location','SouthEast')
% set(gcf,'Color','w')

figure(12)
axis([min(Gr) max(Gr) min(Nu) max(Nu)])
set(gca,'FontSize',15,'FontName','Times')
set(gca,'XMinorTick','on','YMinorTick','on')
```

```
414 xlabel('$Gr = \frac{g\beta(T_s - T_d)V}{\nu^2}$','Interpreter','latex')
415 ylabel('$Nu = \frac{q"A_c^{1/2}}{(T_s - T_d)k}$','Interpreter','latex')
416 title('Nu vs. Gr for F_c = 0')
417 % ap = get(gca,'pos');
418 set(gcf,'PaperPosition',[1 1 7 5.5])
419 set(gcf,'units',get(gcf,'PaperUnits'),'Position',get(gcf,'PaperPosition'))
420 % legend('F_c = 0 (HPo)','F_c = 0.5','F_c = 0.8','F_c = 0.95','Location','SouthEast')
421 set(gcf,'Color','w')
422
423 % figure(13)
424 % set(gca,'FontSize',15,'FontName','Times')
425 % set(gca,'XMinorTick','on','YMinorTick','on')
426 % xlabel('$Gr = \frac{g\beta(T_s - T_d)A_c^{3/2}}{\nu^2}$','Interpreter','latex')
427 % ylabel('$Nu = \frac{q"V^{1/3}}{(T_s - T_d)k}$','Interpreter','latex')
428 % title('Nu vs. Gr for F_c = 0.8')
429 % % ap = get(gca,'pos');
430 % set(gcf,'PaperPosition',[1 1 7 5.5])
431 % set(gcf,'units',get(gcf,'PaperUnits'),'Position',get(gcf,'PaperPosition'))
432 % % legend('F_c = 0 (HPo)','F_c = 0.5','F_c = 0.8','F_c = 0.95','Location','SouthEast')
433 % set(gcf,'Color','w')
434
435 %% Export figure:
436 % figure(1)
437 % export_fig ..\Figures\evaporative_power_vs_V_100.png -r600 -painters
438 %
439 % figure(2)
440 % export_fig ..\Figures\avg_heat_flux_vs_V_100.png -r600 -painters
441
442 % figure(3)
443 % export_fig ..\Figures\avg_volume_100.png -r600 -painters
444 %
445 % figure(4)
446 % export_fig ..\Figures\avg_contact_area_100.png -r600 -painters
447 %
448 % figure(5)
449 % export_fig ..\Figures\avg_temperature_100.png -r600 -painters
```

```
450
451 % figure(6)
452 % export_fig ..\Figures\evap_time.png -r600 -painters
453
454 % figure(7)
455 % export_fig ..\Figures\temp_vs_vol_90.png -r600 -painters
456
457 % figure(9)
458 % export_fig ..\Figures\h_vs_vol_100.png -r600 -painters
459
460 % figure(10)
461 % export_fig ..\Figures\Nu_vs_Gr_VV_80.png -r600 -painters
462 %
463 % figure(11)
464 % export_fig ..\Figures\Nu_vs_Gr_AA_80.png -r600 -painters
465
466 figure(12)
467 export_fig ..\Figures\Nu_vs_Gr_VA_0_power.png -r600 -painters
468
469 % figure(13)
470 % export_fig ..\Figures\Nu_vs_Gr_AV_80.png -r600 -painters
```